Quarterly Report for

Contract DE-FG36-08GO18192

Stanford Geothermal Program

April-June 2011

Table of Contents

1. FRACTURE CHARACTERIZATION USING PRODUCTION DATA

This research project is being conducted by Research Assistant Egill Juliusson, Senior Research Engineer Kewen Li and Professor Roland Horne. The objective is to investigate ways to characterize fractured geothermal reservoirs using production data.

1.1 SUMMARY

Our research on characterizing fractures using production data has led to different ways of estimating connectivity between wells in the reservoir. The focus has been on tracer, pressure and flow rate data, and in the Quarterly Report from Janaury-March 2011 we proposed methods for utilizing these data to optimize injection scheduling in a simple fractured reservoir.

In this quarterly report we describe a test of the optimization procedure that aims to maximize the net present value of production on the Soultz reservoir model, which has a relatively complex fracture network with four injectors and three producers. In the first case we optimized only the injection rates, but the production rates were determined by a constant bottomhole pressure condition. The results indicate that considerable gains can be made by optimizing the injection schedule. The thermal breakthrough predictions defined in the optimization procedure are based on an analytical formulation (Lauwerier, 1955), and these matched the simulated thermal breakthrough surprisingly well, considering that the fracture apertures used in the formulation were poorly calibrated.

For the second case we developed a method for computing the flow rate based interwell connectivity when both injection and production rates are controlled. We then proceeded to optimize both the injection and production rates for the Soultz reservoir model. Although the optimization procedure seemed to work without problems, the predicted thermal breakthrough did not match the simulated values very well.

A likely reason for this is that the effective fracture aperture, or alternatively, the effective heat transfer area, is poorly constrained by the production data that our method is based on. One way to achieve a better estimate of these parameters would be to collect thermal breakthrough data and then fit the analytical breakthrough curves to those data. This, however, would require an analytical formulation of the thermal breakthrough under variable flow rate conditions, which is a topic left for further study.

1.2 INTRODUCTION

Understanding interwell connectivity is a requirement for geothermal field management. For example, premature thermal breakthrough can be prevented if an injector-producer pair is known to be well connected (and therefore can be avoided). A quantitative way of defining the connectivity leads to the possibility of optimizing reinjection scheduling (Lovekin and Horne, 1989).

Juliusson and Horne (2010) discussed a quantitative way of determining injector-producer connectivity from tracer tests. The connectivity was defined in terms of a convolution kernel representative of the flow paths connecting each injector-producer pair. A method for estimating these kernels was developed, at steady-state flow conditions. The

observation was made that the kernels do not apply for all flow rate conditions and were therefore of limited use for reinjection scheduling.

A way to account for the variability in flow rates was discussed by Juliusson and Horne (2011). The key addition was that the convolution kernels were represented in terms of cumulative flow, and could therefore be applied at variable flow rate conditions. The mathematical basis for the method depended on the one-dimensional advection-dispersion equation. The method works remarkably well for flow through naturally fractured reservoirs because the stream lines are constrained by the largest fractures in the reservoir.

In the Quarterly Report from January-March 2011 the variability of tracer returns as a function of flow rate was tested further by developing a flow model with data from the Soultz enhanced geothermal system. Tracer simulations in the model showed that the tracer kernel method worked well for those injector-producer pairs that were strongly connected. A few different options for using tracer data to optimize reinjection schedule were introduced and tested with a simple model of two injectors and two producers.

In this quarter we tested the optimization procedure that aims to maximize the net present value of production on the Soultz reservoir model, which has a relatively complex fracture network, with four injectors and three producers. In the first case we optimized the only the injection rates and the production rates were determined by a constant bottomhole pressure condition. For the second case we developed a method for computing the interwell connectivity when both injection and production rates are controlled, and then proceeded to optimize both the injection and production rates for the Soultz reservoir model.

1.3 OPTIMIZATION OF INJECTION SCEHDULING FOR THE SOULTZ RESERVOIR MODEL

In the quarterly report from January-March 2011, we described the development of a flow model based on data obtained from the Soultz-sous-Forêts enhanced geothermal system in France. The model included four injection wells and three production wells. Snapshots of tracer distribution in the model after 300 days of continuous injection into each injector are shown in Figure 1.1. Tracer flow simulations were run under various flow conditions to investigate the variability in tracer returns with flow rate. These flow rate and tracer data were then used to determine the interwell connectivity (IWC), tracer kernel, and effective pore volume between each injector-producer pair. A description of how these data were used to predict thermal breakthrough and optimize the injection strategy for the field follows.

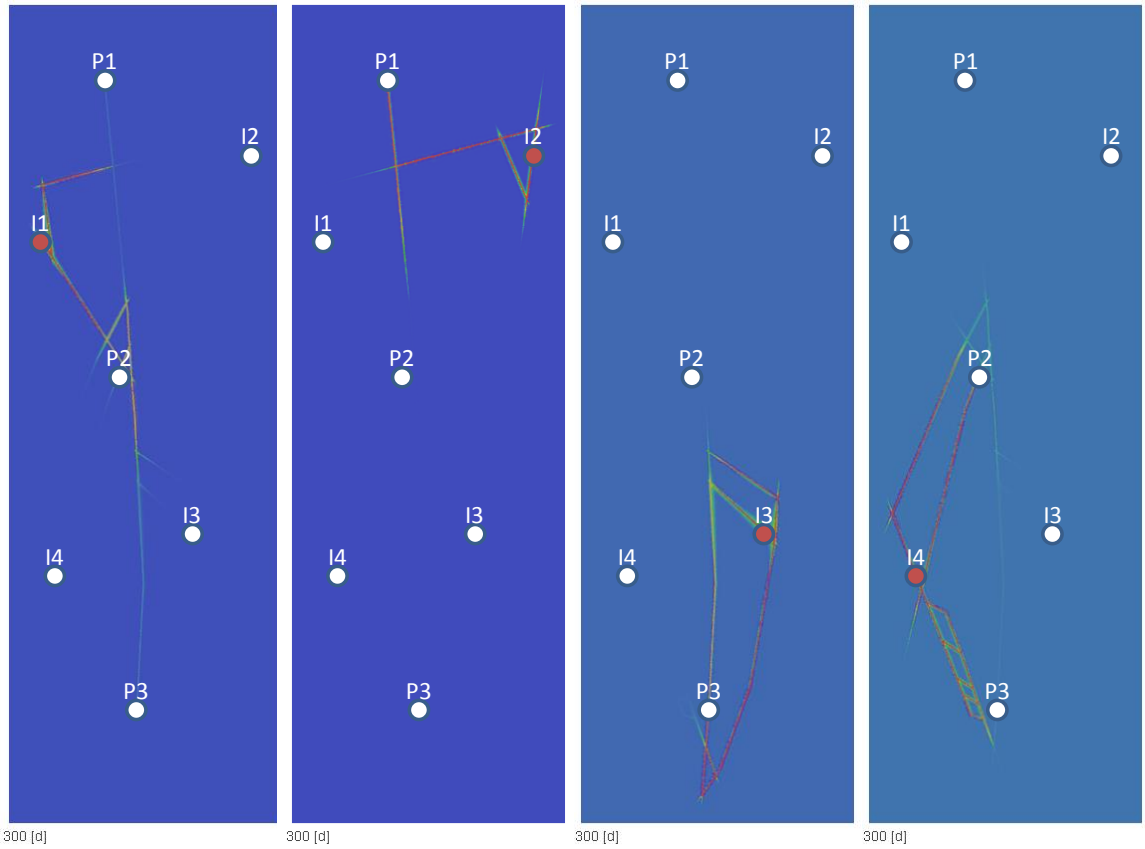

Figure 1.1: The tracer distribution in the reservoir after 300 days of tracer injection, into wells I1 through I4, going from left to right. The injection rate was 3000 m^3/day for each injector.

We assumed that some porosity estimates and wellbore imaging data were available (as is the case for the Soultz reservoir) which would be helpful for guessing the approximate fracture aperture. Any additional reservoir information from the underlying model was ignored. Hence, this was a test of how well an optimization would perform based on data that could be measured in the field using well established methods, without the use of a traditional reservoir simulator.

The objective function we used for this test focused on maximizing the net present value of production from the reservoir. An empirical correlation was used to compute the specific power output as a function of the injection and production temperature. The correlation, found by Bennett and Horne (2011), was based on results presented in the MIT report (Tester et al., 2006, Figure 7.3). The specific power output, in units of kW/(m^3/day), was:

$$\tilde{z}_j(T_{Pj},T_I) = 3.854\times10^{-5}(T_{Pj}-\zeta)^2 - 1.268\times10^{-3}(T_{Pj}-\zeta) - 2.123\times10^{-2} \qquad (2.1)$$

with

$$\zeta = 0.563T_I - 14.51 \tag{2.2}$$

and temperatures taken in °C. Water density was assumed to be 900 kg/m^3 when converting the correlations to volumetric units.

In practice, power plants are designed to work at a given temperature range. To include this consideration, a minimum temperature threshold was added to the power output correlation. This threshold had to be modeled by a smooth function to avoid complications in the optimization procedure. Thus, we defined the specific power output as:

$$z_j(T_{Pj}(t,\bar{q}_I),T_I,T_{P\min}) = \frac{1}{2}(erf(T_{Pj}(t,\bar{q}_I) - T_{P\min}) + 1)\tilde{z}_j(T_{Pj}(t,\bar{q}_I),T_I) \tag{2.3}$$

where *erf* denotes the error function and T_{Pmin} denotes the minimum design temperature threshold. The specific power output curve is plotted as a function of production and injection temperature, with a design threshold of 120°C, in Figure 1.2.

The net present value of producing from the reservoir was then computed as:

$$O(\bar{q}_I) = \sum_{j=1}^{N_P} \int_0^{t_f} P(t) z_j\left(T_{Pj}(t,\bar{q}_I),T_I\right) \bar{q}_{Pj}(t,\bar{q}_I) e^{-rt} dt \tag{2.4}$$

where *P(t)* denotes the unit price of energy and *r* denotes the chosen discount rate for the investment. T_{Pj} was computed using Equation (1.11) in the Quarterly Report from January-March 2011.

The optimal injection strategy was found by minimizing *O* in Equation (2.4). As mentioned earlier, it was assumed that estimates of flow rate-based IWCs and tracer kernels were available. We also assumed that some core samples were available, along with wellbore imaging logs that would give an idea about the aperture and porosity of the fractures we were looking at. Otherwise, we tried to ignore any additional knowledge we had about the reservoir.

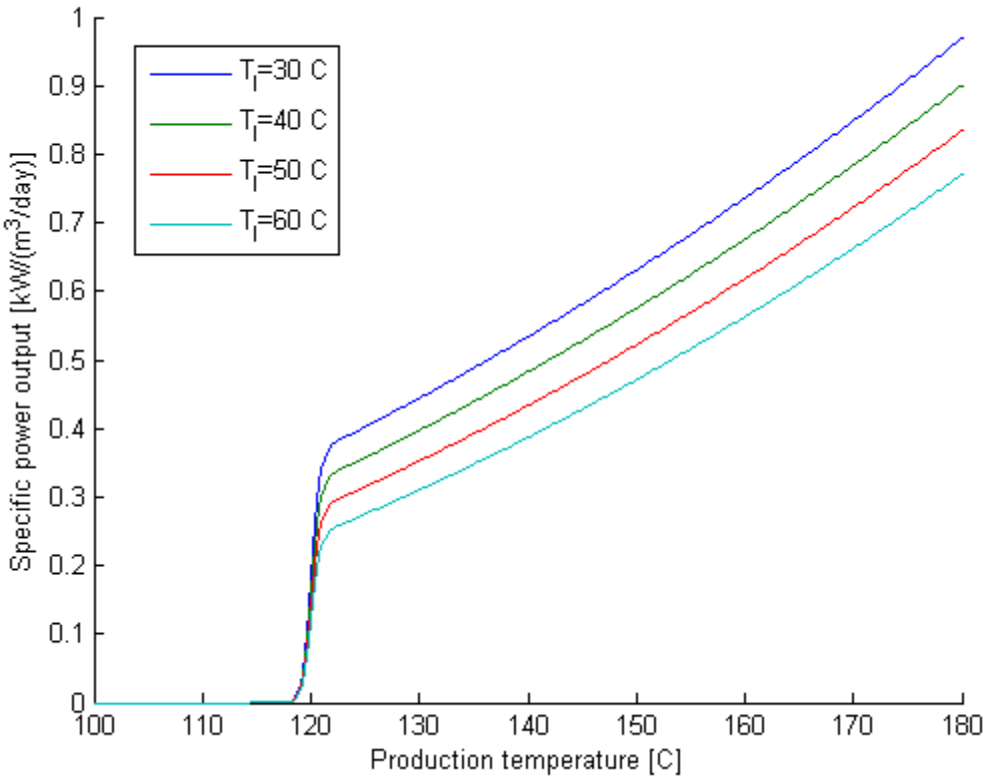

Figure 1.2: Specific power output correlation as a function of injection and production temperature. A minimum design temperature threshold of 120 C was applied in this case.

The average of the flow rate and tracer-based IWCs was used to compute the injector-producer flow rates (Table 1.1).

Table 1.1: Interwell connectivity (IWC) parameters used for optimization. These are the average values of those parameters estimated by flow rate variations and tracer returns.

IWC≡F	I1	I2	I3	I4
P1	0.201	0.876	0.022	0.031
P2	0.692	0.103	0.052	0.869
P3	0.056	0.030	0.971	0.080

Direct estimation of the pore volumes using these IWCs gave the volume estimates shown in Table 1.2.

Table 1.2: Estimated pore volume using IWC parameters from Table 1.1and tracer returns with flow distributed evenly between all injectors. Inadequate estimates are labeled in yellow.

Vx [m^3]	I1	I2	I3	I4
P1	17,116	27,807	8,263	5,776
P2	21,419	75,070	17,086	39,768
P3	10,423	24,325	59,393	18,229

The inadequate pore volume estimates corresponded to cases where relatively little tracer had been recovered. This did not necessarily mean that there was no fracture connection between the wells in question. It could have been that the measurement time was not long enough, because the flow rate was low, as indicated by the IWC estimates. Thus, we used the good connections to compute an average pore volume per distance between wells. This yielded $V_x/L \approx 48$ m^2, which lead to the estimated pore volumes shown in Table 1.3.

Table 1.3: Estimated pore volumes used for optimization.

Vx [m3]	I1	I2	I3	I4
P1	17,116	27,807	79,572	85,899
P2	21,419	43,908	29,001	39,768
P3	82,304	97,164	59,393	18,229

The ratio of the pore volume, $V_{x,ij}$, to the IWC, F_{ij}, could be used as an indicator of the time until thermal breakthrough (Table 1.4). This can be seen by writing out the Lauwerier (1955) solution in the form:

$$T_{D,ij}(t,q_{Ii}) \approx erfc\left(\frac{\xi_{ij}}{2\sqrt{\theta\tau_{ij}}}\right) = erfc\left(\frac{V_{x,ij}}{F_{ij}q_{Ii}R\phi_f\,2b_{ij}}\sqrt{\frac{K_r\rho_{am}c_{am}}{(\rho_w c_w)^2 t}}\right) \tag{2.5}$$

The pore volume to IWC ratio indicated that the largest interaction would be between well pairs *P1-I2*, *P2-I1*, *P2-I4*, and *P3-I3*.

Table 1.4: Ratio of pore volume to IWC estimated for the optimization problem.

Vx/F	I1	I2	I3	I4
P1	85,015	31,733	3,595,986	2,735,735
P2	30,949	428,119	561,737	45,775
P3	1,464,266	3,230,772	61,180	227,084

Equation (2.5) shows that the principal remaining uncertainty is with the group $R\varphi_f b_{ij}$. In practice, some average estimate for the fracture and matrix porosity might be obtainable from core sampling, but determining the effective aperture, b_{ij}, would be challenging. For lack of a better method we simply took $b_{ij} = 1$ m, as a value that might seem to be of the

right order of magnitude based on well bore imaging. Other ways to estimate aperture are described in Section 4 of this report. Assuming that the core data had given $\varphi_m = 0.001$ and $\varphi_f = 0.04$, we then had all the parameters required for Equation (2.5).

The optimization was performed using the IWCs and pore volumes given in Table 1.1 and Table 1.3, respectively. A 4500 m^3/day upper bound constraint was applied to the individual injection rates, and a 12000 m^3/day total injection constraint was used. As before, the interest rate was r=8% and the energy price was increasing over a 30 year period in real terms, from 60 to 120 $/MWh with an added 2% inflation. The optimal injection rates, based on these assumptions, are shown in Table 1.5.

Table 1.5: Optimal injection rates for the Soultz reservoir model.

Well	[m3/day]	
I1	1,225	20%
I2	1,244	20%
I3	2,145	35%
I4	1,516	25%
ΣIi	6,130	100%

The objective function could not be plotted in this case, as it was four-dimensional. We could, however, view slices of the objective function with two of the decision variables fixed at the optimal values. Figure 1.3 shows a q_{I1}-q_{I2} slice of the objective function with q_{I3} and q_{I4} fixed at the optimal values. These plots were useful to verify that the optimization algorithm had not become trapped in a local maximum.

The value of the objective function, based on the analytical temperature estimates, increased by 37% compared to the initial allocation of 3000 m^3/day per well. However, it is more meaningful to look at the improvement based on the simulations, since they were meant to represent the actual outcome of the injection strategy. The simulation based NPV for the initial allocation was 19.7 M$, while the optimized allocation yielded 25.2 M$. Thus, a 27% increase was obtained over the initial allocation.

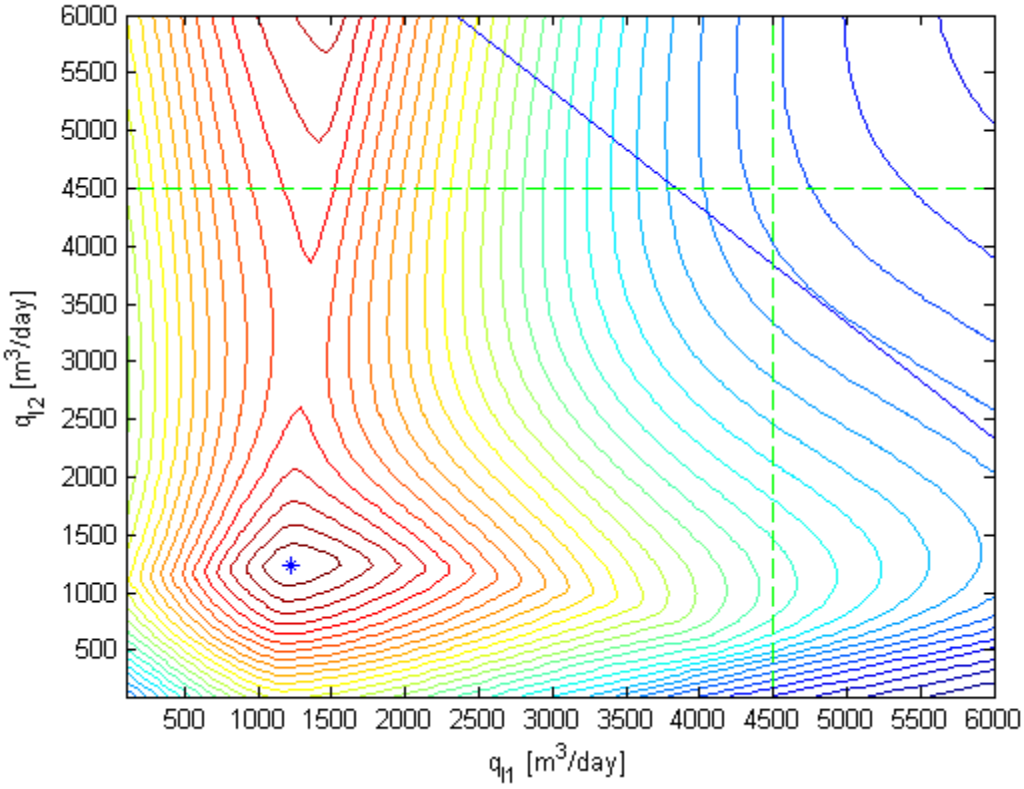

Figure 1.3: A contour plot of a slice through the objective function based on net present value of production. The slice is taken with q_{I3} = 2145 m^3/day and qI4 = 1516 m^3/day, which are the optimum values. A maximum total injection constraint of 12000 m^3/day is illustrated by the blue diagonal line. Maximum injection constraints of 4500 m^3/day for injectors I1 and I2 are shown by the green dashed lines. The optimum feasible point is shown by the blue star.

The predicted and simulated thermal breakthrough curves are shown in Figure 1.4 for the case when the flow was distributed evenly at 3000 m^3/day to each injector. The same curves for the optimal injection rates are shown in Figure 1.5.

The predicted and simulated breakthrough curves matched surprisingly well, especially for the even injection case. This good match was probably somewhat coincidental because the aperture value was chosen rather arbitrarily. Better ways to characterize the fracture aperture are needed, but are hard to find (see Section 4).

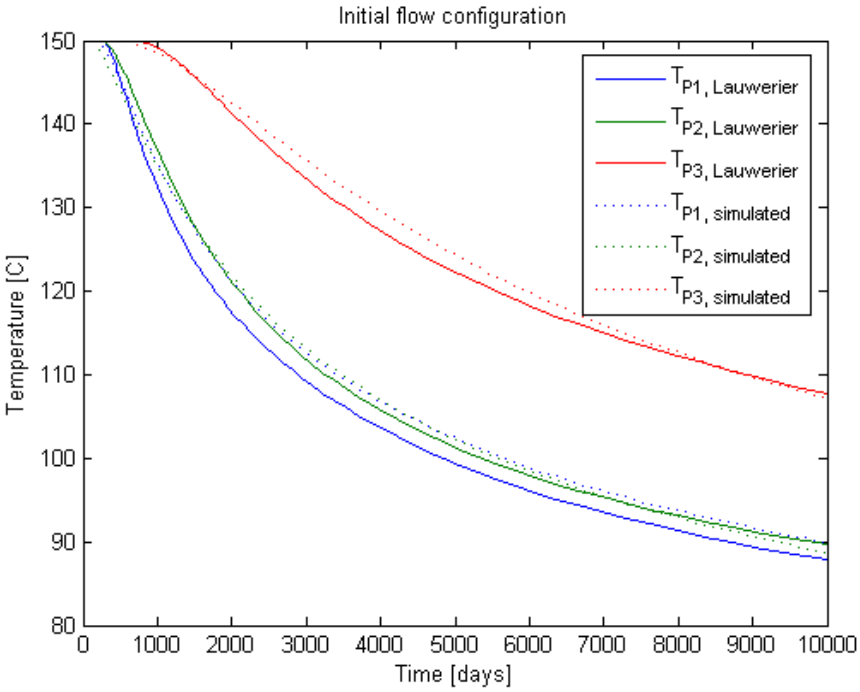

Figure 1.4: Comparison of simulated thermal breakthrough and thermal breakthrough as predicted by the Lauwerier (1955) analytical model. For this case water at 50°C was injected at 3000 m^3/day into each of the four injectors.

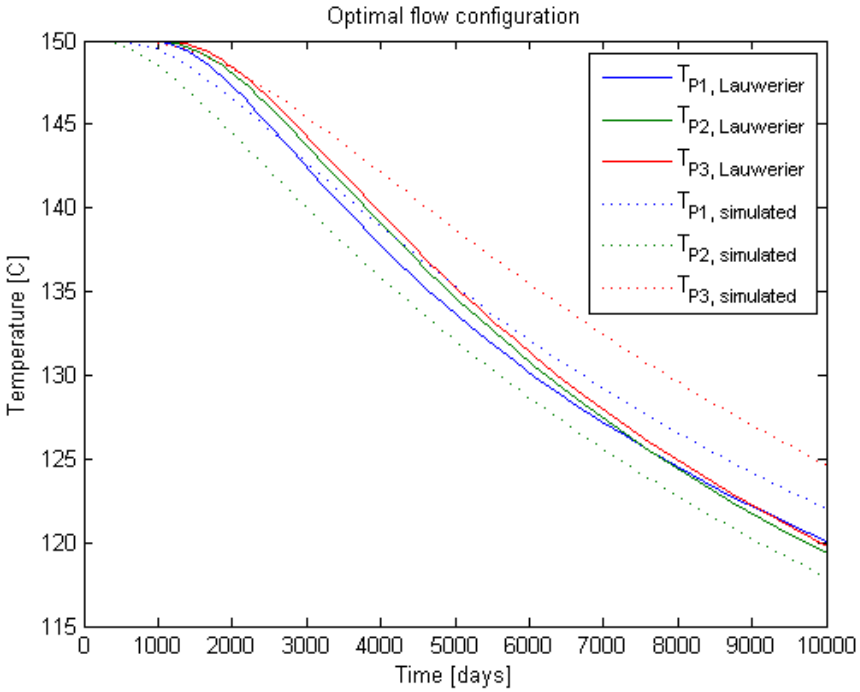

Figure 1.5: Comparison of simulated thermal breakthrough and thermal breakthrough as predicted by the Lauwerier (1955) analytical model. For this case water at 50°C was injected at the optimal flow rates given in Table 1.5.

1.4 FLOW RATE BASED CONNECTIVITY FOR VARIABLE INJECTION AND PRODUCTION CONDITIONS

The optimization procedures we have had under investigation thus far have focused on injection rates, whereas production rates have been determined by a constant bottom hole pressure condition. Thus the production rates have been functions of the injection rates.

In practice one might want to take advantage of being able to control both the injection and production rates. This in turn requires a change in the way we have defined the flow rate based IWC, such that it can apply at any given production rate. To make this possible, we developed a technique where a set of flow rate and pressure data was used to determine the effective transmissibility between each well pair. Thus the effective injector-producer flow rate could be computed, along with production rate dependent interwell connectivity. A description of the method follows.

To find the transmissibility we assume we have a closed reservoir with incompressible flow. Then we write the following volume balance equation for each well:

$$q_i = \sum_{j \neq i} q_{ij} = \sum_{j \neq i} \alpha_{ij} (p_j - p_i) \tag{2.6}$$

where α_{ij} denotes the effective transmissibility, and p denotes the pressure. This can be written as a vector-matrix product, i.e.:

$$\bar{q} = A\bar{p} \tag{2.7}$$

where

$$A = \begin{pmatrix} -\sum_{j \neq 1} \alpha_{1j} & \alpha_{12} & \cdots & \alpha_{1N_w} \\ \alpha_{21} & \ddots & & \vdots \\ \vdots & & \ddots & \alpha_{N_w-1 N_w} \\ \alpha_{N_w 1} & & \alpha_{N_w N_w-1} & -\sum_{j \neq N_w} \alpha_{N_w j} \end{pmatrix} \tag{2.8}$$

In this formulation it is assumed that the pressures and flow rates are at a steady state, and therefore the measurements used to derive the transmissibilities should be taken after the pressure transients have stabilized. An example data set was created in the groundwater simulation software FEFLOW using the Soultz model. The flow rate was changed every 10 days and measurements taken just before the change were used to infer *A*. The matrix *A* was constrained to have the structure defined by Equation (2.8), where $\alpha_{ij} = \alpha_{ji}$. Logs of the controlled flow rate are shown in Figure 1.6. The resulting pressure changes are shown in Figure 1.7. Data from the first 150 days were used to infer *A*, and then the pressure was predicted and compared to simulated values over the next 150 day period. The relative error in these predictions was approximately 8%. To establish some sort of baseline for the

pressure values, it was necessary to assume that the average pressure in the reservoir remained constant. Thus, the pressure predictions were obtained from:

$$\bar{p} = \begin{bmatrix} A \\ \bar{1} \end{bmatrix}^{-1} \begin{bmatrix} \bar{q} \\ p_{ave} \end{bmatrix} \tag{2.9}$$

where p_{ave} was the average measured pressure in the reservoir.

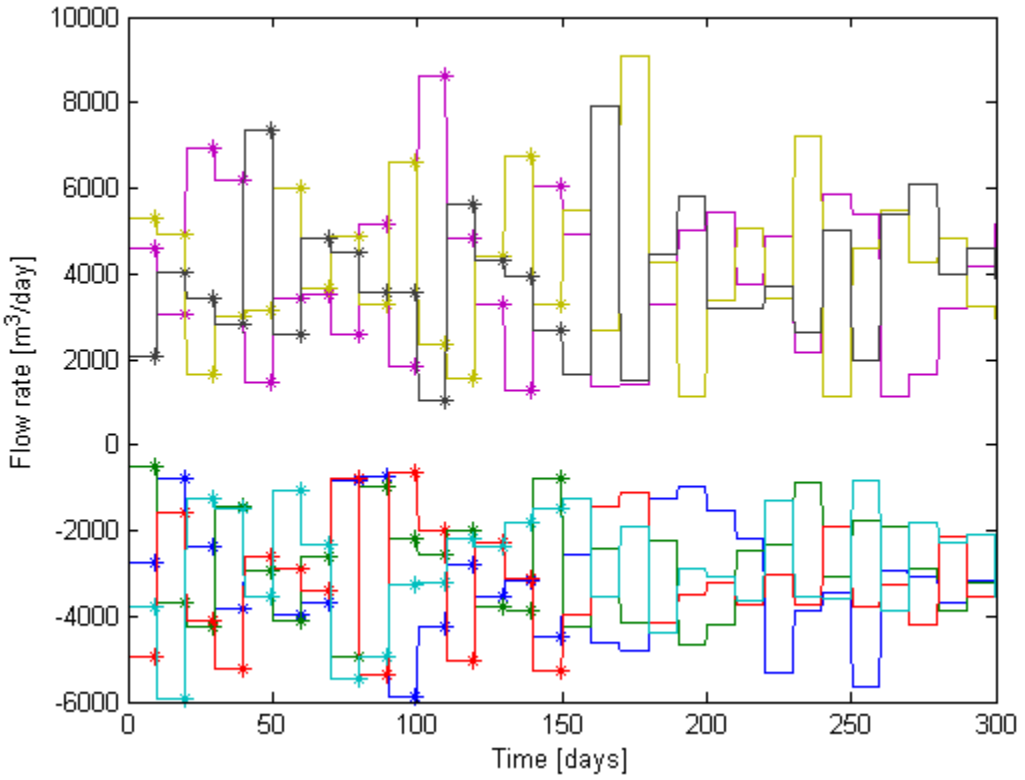

Figure 1.6: A random set of forced injection and production rates used in the Soultz model. Injection rates are negative, production positive. The stars denote the points that were used to calibrate the transmissibility estimates.

With this estimate of A the pressures and thereby the interwell flow rates, q_{ij}, could be predicted. To find the injector-producer flow rates, q_{IiPj}, it was necessary to account for the net inflow into each injection and production well. This was done by solving the equivalent flow network problem, where all paths from each injector to each producer needed to be found. The solution routine was similar to that described in the Quarterly Report from January-March 2010 (Section 1.3.3). The IWCs were computed as

$$F_{ij}(\bar{q}_I, \bar{q}_P) = \frac{q_{IiPj}}{q_{Ii}} \tag{2.10}$$

The transmissibilities obtained from this method are illustrated in Figure 1.8. The same figure shows the IWCs for a given set of injection and production rates. The IWCs from this method could be compared to those obtained by the M-ARX method (see Quarterly Report from January-March 2011) by setting the production rates to the values they would have had if the bottomhole pressure were fixed. We performed a few such comparisons which showed that the resulting IWCs were essentially the same (discrepancies were around 1-3%).

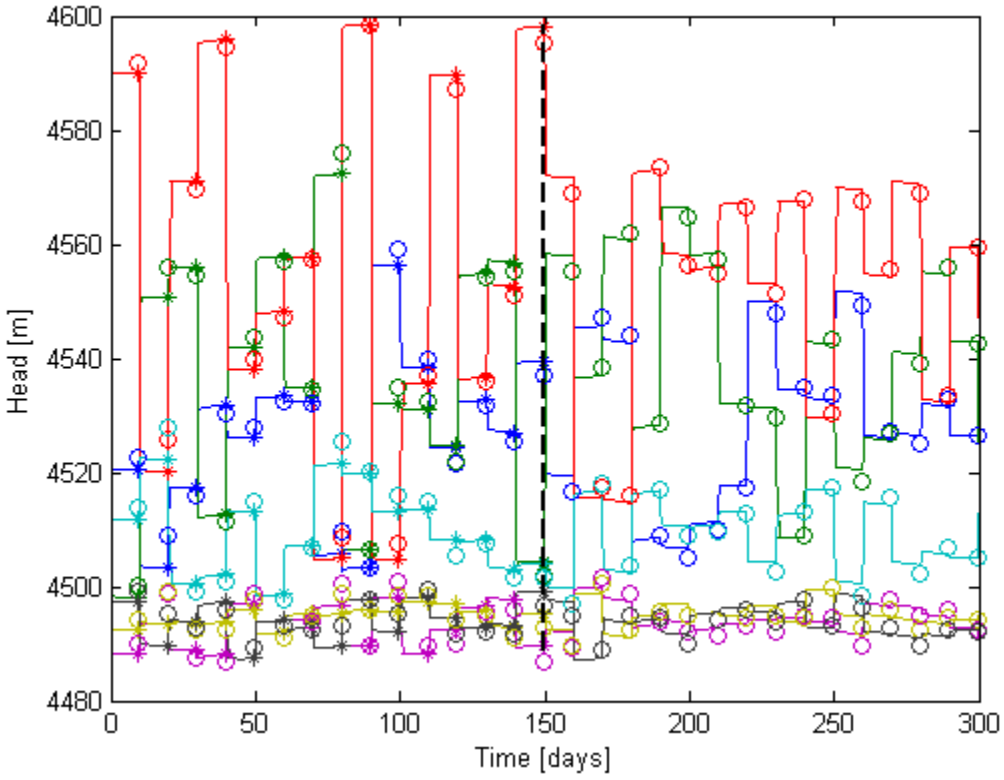

Figure 1.7: Bottomhole pressure logs resulting from the variations in injection and production rates shown in Figure 1.6. The stars denote the points that were used to calibrate transmissibility estimates, and the circles denote the predicted pressure.

We point out that what is described here is a generalization of other methods for computing interwell connectivity (see e.g. Lee et al., 2010 and Dinh, 2009), which allows both the control of injection and production rates. It comes at the cost of having to have measurements of both bottomhole pressure and flow rates, and it is particularly useful when estimates of the effective flow rate between each injectior-producer pair is required as a function of both injection and production rate.

In the next section we describe how this method was applied to optimize both the injection and production rates for the Soultz reservoir model.

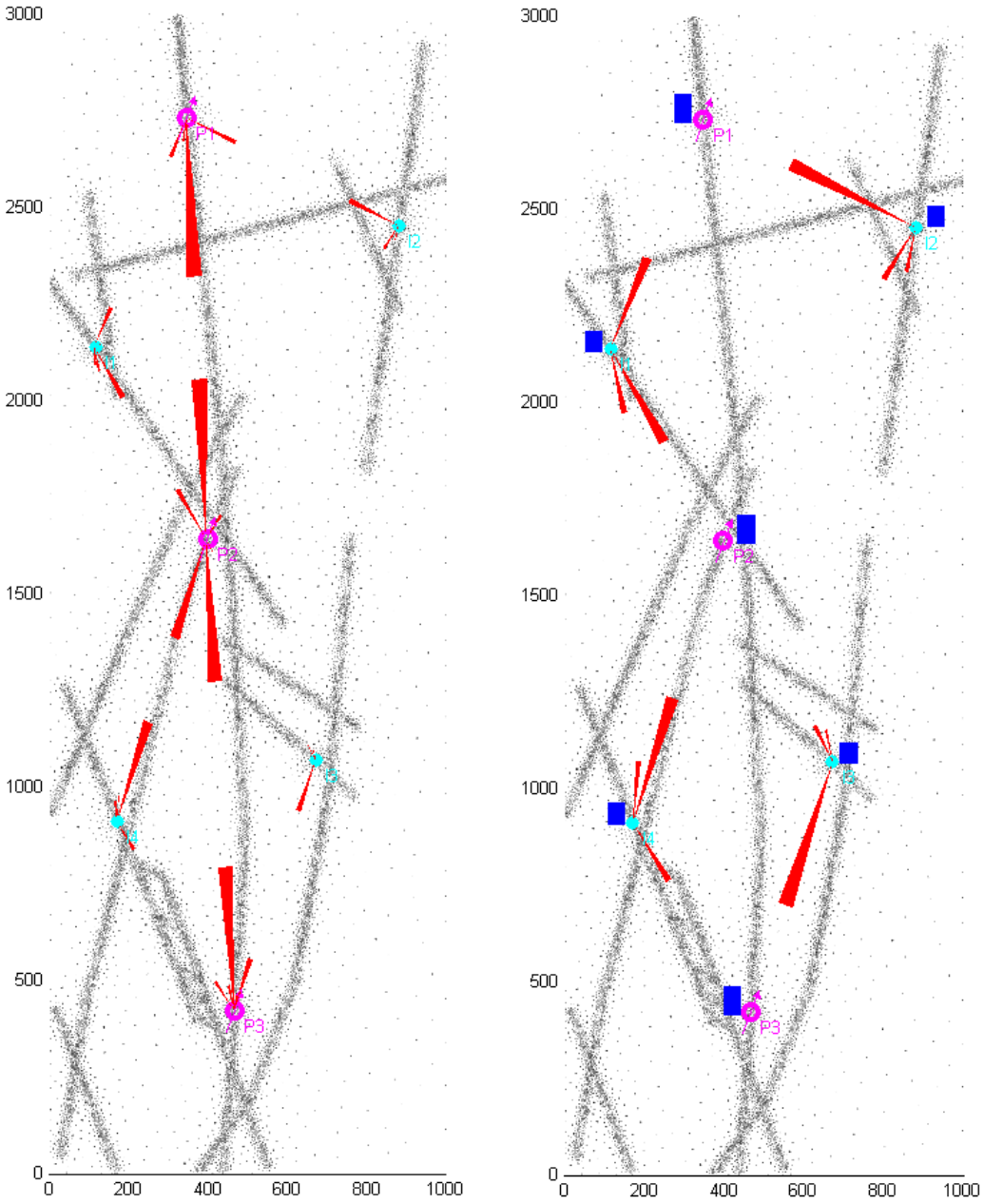

Figure 1.8: The left part of this figure illustrates the well-to-well transmissibilities as proportionately sized red triangles. The right side shows the interwell connectivity for each injector producer pair (red triangles) given evenly distributed injection and production rates (blue rectangles). The gray dots in the background, which are the vertices of the FEFLOW grid, are included to outline the fractures in the reservoir.

1.5 OPTIMIZATION OF INJECTION AND PRODUCTION SCEHDULING FOR THE SOULTZ RESERVOIR MODEL

With the development of production rate dependent IWC it was possible to optimize both the injection and production rates for the Soultz reservoir. In this case the objective function was defined as:

$$O(\bar{q}_I,\bar{q}_P)=\sum_{j=1}^{N_P}\int_0^{t_f}P(t)z_j\left(T_{Pj}(t,\bar{q}_I,\bar{q}_P),T_I\right)\hat{q}_{Pj}(t)e^{-rt}dt \tag{2.11}$$

where

$$z_j(T_{Pj}(t,\bar{q}_I,\bar{q}_P),T_I,T_{P\min})=\frac{1}{2}(erf(T_{Pj}(t,\bar{q}_I,\bar{q}_P)-T_{P\min})+1)z_j(T_{Pj}(t,\bar{q}_I,\bar{q}_P),T_I) \tag{2.12}$$

and

$$T_{Pj}(t,\bar{q}_I,\bar{q}_P)=\sum_{i=1}^{N_I}w_{ij}(\bar{q}_I,\bar{q}_P)\left(T_0-(T_0-T_I)T_{D,ij}(t,\bar{q}_I,\bar{q}_P)\right) \tag{2.13}$$

Within Equation (2.13) we have:

$$T_{D,ij}(t,\bar{q}_I,\bar{q}_P)=erfc\left\{\left(\frac{(\rho_a c_a)^2}{K_r\rho_r c_r}\left(\frac{\phi b q_{IiPj}}{V_{x,ij}}\right)^2\left(t-\frac{\rho_a c_a}{\rho_w c_w}\frac{V_{x,ij}}{\phi q_{IiPj}}\right)\right)^{-0.5}\right\} \tag{2.14}$$

which depends on all the injection and production rates because:

$$q_{IiPj}=q_{Ii}F_{ij}(\bar{q}_I,\bar{q}_P) \tag{2.15}$$

The nomenclature here is the same as in the Quarterly Report from January-March 2011.

Solving the maximization problem for Equation (2.11) yielded the injection and production rates given in Table 1.6 and Table 1.7. From these results it seems that the optimal strategy would be to pull a relatively large amount of water through the middle producer (P2) by injecting mostly into wells I2 and I3, which have poor connections to P2. The flow rate for I1 is kept relatively small to avoid premature cooling in P2.

Table 1.6: Optimized injection rates for the case where both injection and production are controlled.

Well	[m3/day]	
I1	1241	13%
I2	4080	43%
I3	2216	23%
I4	1897	20%
ΣIi	9434	100%

Table 1.7: Optimized production rates for the case where both injection and production are controlled.

Well	[m3/day]	
P1	1130	12%
P2	4714	50%
P3	3589	38%
ΣPj	9434	100%

The thermal breakthrough predictions made by the analytical formulations (2.13) and the actual simulation are shown in Figure 1.9 and Figure 1.10. Figure 1.9 shows the predictions for the default scenario were 12000 m^3/day were distributed evenly between the wells (3000 m^3/day per injector, 4000 m^3/day per producer). Figure 1.10 shows the predictions at the optimal flow rate configuration.

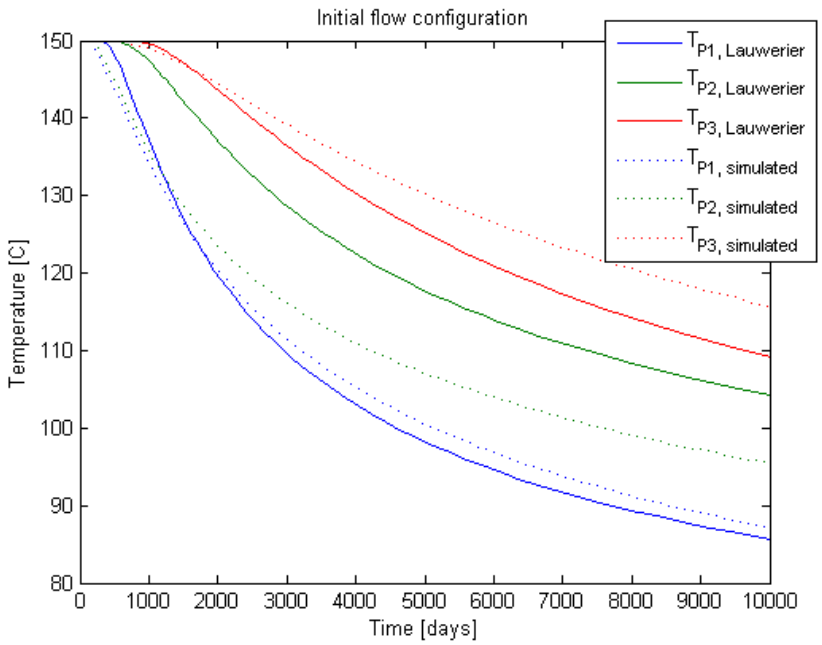

Figure 1.9: Predictions for thermal breakthrough for the case where injection and production rates are distributed evenly. The predictions made by Equation (2.13) are shown by solid lines and the simulated predictions are shown by the dotted lines.

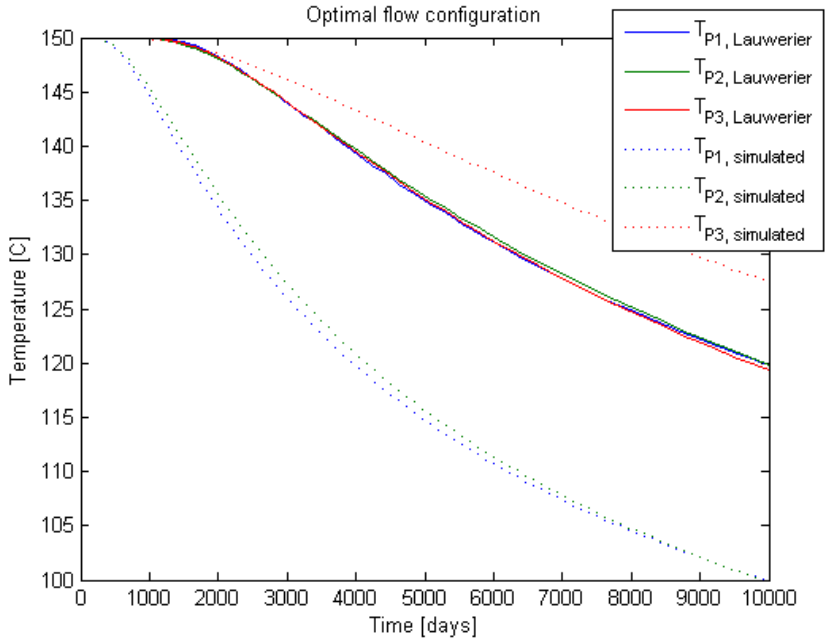

Figure 1.10: Predictions for thermal breakthrough for the case where injection and production rates have been optimized. The predictions made by Equation (2.13) are shown by solid lines and the simulated predictions are shown by the dotted lines.

First we point out that in this case, the thermal breakthrough curves coincide at the optimal flow configuration, which was not possible in the case where only the injection rates were controlled the as seen in Figure 1.5. This result seems intuitive and in line with previously defined objectives for reinjection scheduling.

A more concerning matter is that the simulated thermal breakthrough does not match the thermal breakthrough as predicted by Equation (2.13). This means that some additional measures must be taken to either revise the formulation or obtain more accurate data. These formulations rely on estimation of the fracture aperture. An alternative to finding the fracture aperture would be to estimate the effective heat transfer area of the flow path. For example, Equation (2.14) can be written in terms of the effective heat transfer area, $A_{x,ij}$, as follows:

$$T_{D,ij}(t,\bar{q}_I,\bar{q}_P) \approx erfc\left\{\frac{A_{x,ij}}{q_{IiPj}}\sqrt{\frac{K_r\rho_a c_a}{(\rho_w c_w)^2 t}}\right\} \tag{2.16}$$

This way one could avoid having to determine the fracture volume and aperture and focus on ways to determine the size of the fracture surface, e.g., based on seismic imaging or reactive tracers, or by fitting analytical models to thermal breakthrough data.

1.6 FUTURE WORK

The parameters $A_{x,ij}$ could be predicted by collecting the thermal breakthrough data and fitting Equation (2.13) to the measurements. Although the uniqueness of such a solution is questionable it seems worthwhile to investigate that alternative. Especially since those $A_{x,ij}$ values corresponding to high interwell connectivity values should be most influential for the solution. In that case the optimal flow configuration could be updated after enough thermal breakthrough data has been obtained to reevaluate $A_{x,ij}$. This leads to the need for an analytical equation for thermal breakthrough under variable flow rate conditions. An investigation of such solutions will be the subject of the next Quarterly Report.

2. FRACTURE CHARACTERIZATION OF ENHANCED GEOTHERMAL SYSTEMS USING NANOPARTICLES

This research project is being conducted by Research Associates Mohammed Alaskar and Morgan Ames, Senior Research Engineer Kewen Li and Professor Roland Horne. The objective of this study is to develop in-situ multifunction nanosensors for the characterization of fractures in Enhanced Geothermal Systems (EGS).

2.1 SUMMARY

During this quarter we began investigation of microparticle flow in fractures. Preliminary investigation of the flow mechanism of nanoparticles through a naturally fractured greywacke core was conducted by injecting fluorescent silica microspheres. We found that silica microspheres of different sizes (smaller than fracture opening) could be transported through the fracture. We demonstrated the possibility of using microspheres to estimate fracture aperture by injecting a polydisperse microsphere sample. It was observed that only spheres of 20 μm and smaller were transported. This result agreed reasonably well with the measurement of hydraulic fracture aperture (27 μm) as determined by the cubic law.

We also began experiments to investigate the feasibility of magnetic collection of nanoparticles from produced fluid. It was estimated using UV-vis spectroscopy that 3% of the injected nanoparticles were recovered in a prototype magnetic collection device.

2.2 INTRODUCTION

In the previous quarter (January–March, 2011), a naturally fractured greywacke core from The Geysers was prepared for the injection of fluorescent silica microspheres. The preparation of the fractured core included the estimation of the hydraulic aperture and permeability of the fracture. The fluorescent silica microsphere samples were characterized in terms of size, shape, zeta potential and light emission using optical and scanning electron microscopy (SEM), Zetasizer and fluorescence spectrometer, respectively. Prior to the injection of the silica microspheres, silicon dioxide nanoparticles were characterized and injected into the fractured core as a base-line measurement. The effluents were analyzed using dynamic light scattering (DLS) and SEM. The silicon dioxide (SiO_2) nanoparticles flowed through the fractured greywacke core successfully.

During this quarter, the silica microspheres of different sizes were injected into the naturally fractured greywacke core sample. The effluent samples were analyzed using optical microscopy and fluorescence spectrometer. The fluorescence intensity was related to effluent concentration by constructing a calibration curve. The return curve was then estimated.

2.3 CHARACTERIZATION OF FRACTURED GREYWACKE

The core sample tested was a fractured greywacke from The Geysers geothermal field, with 5.08 cm diameter and 3.01 cm length. The core sample was fitted between the two end-pieces and wrapped with Teflon shrink tube. An electric heating gun was used to bond

the assembly together. To achieve proper sealing, the heat was applied evenly starting from the bottom up using a circular motion. The assembly was positioned horizontally and polyethylene tubes (0.3175 cm in diameter) and fittings were used to connect the water pump and pressure manometer to the core assembly. As only a very low differential pressure was required to flow fluid through the fractured core, the inlet pressure was measured using a manometer tube rather than a transducer. The flow rate was measured using a balance and stop watch. The hydraulic aperture of the fracture was determined using the cubic law. The average of the hydraulic aperture of the fracture was found to be approximately 27 μm. The average permeability of the rock was found to be 60 darcy. Further details of the experimental apparatus and core characterization can be found in the previous quarterly report (January-March, 2011).

2.4 FLUORESCENT SILICA MICROSPHERES: CHARACTERIZATION AND INJECTION EXPERIMENT

The objectives of this experiment were to investigate the transport and recovery of fluorescent silica microspheres through fractures, by using a greywacke core sample and to study the relationship between the size of recovered microparticles and fracture aperture. As a base-line experiment, initial testing was conducted by injecting silicon dioxide (SiO_2) nanoparticles, which we had earlier shown to be transported successfully in other rocks. Given that the silicon dioxide nanoparticles had been transported successfully through Berea sandstone, our first step in the fracture experiments was to test their delivery through the fractured greywacke core sample. The purpose was to determine if the greywacke core material would impose any constraint on the recovery of silica based nanoparticles, prior to the injection of the fluorescent silica microspheres.

2.4.1 Characterization of fluorescent silica microspheres

Fluorescent silica microspheres were characterized in terms of size and shape, zeta potential and light emission (fluorescence). The zeta potential measurement was not possible because of the quick settlement of the silica microparticles at the bottom of the measurement cell (due to their size) during the analysis, leading to erroneous measurements. The size and shape of the microspheres were characterized using an optical microscope and scanning electron microscope (SEM). The emission spectrum was obtained using a fluorescence spectrometer.

Optical and scanning electron images of the microsphere samples are shown in Figure 2.1. The blue and green samples were shown to have uniformly sized spheres with an average particle size of about 2 and 5 μm, respectively. The red silica spheres were polydisperse or polysized. The red sample has spheres with diameters ranging from 5 to 31 μm.

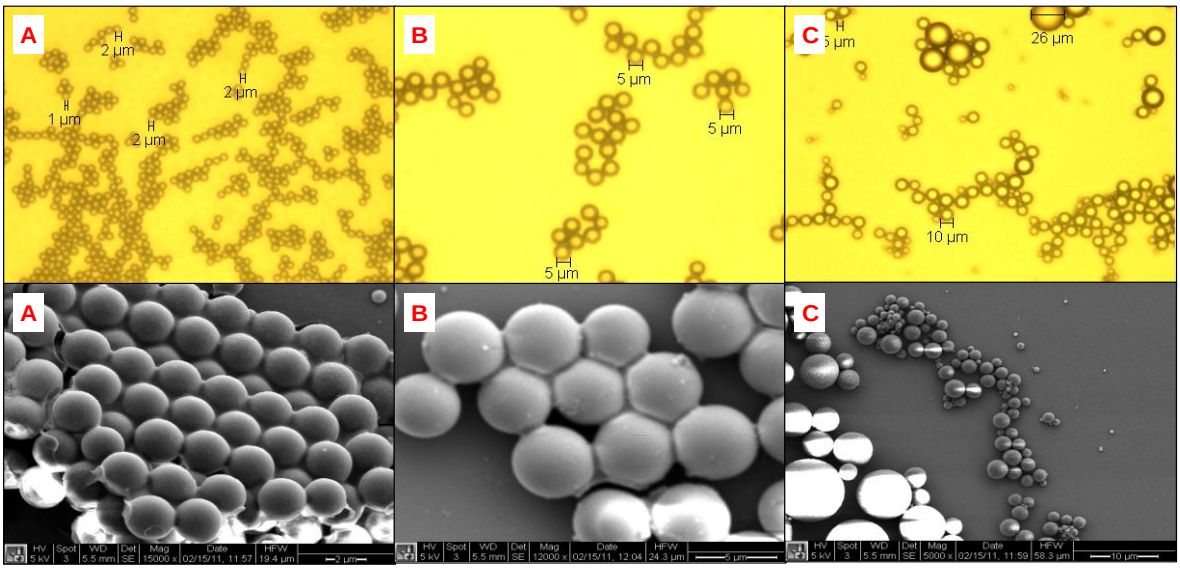

Figure 2.1: Optical and SEM images of (A) blue, (B) green and (C) red silica microspheres.

The volume of blue, green and red fluorescent silica samples was five cubic centimeters with concentration of five percent. The density of the sample was measured in the laboratory at temperature of 24.5ºC. An accurate pipette was used to obtain one cubic centimeter of microfluid at original concentration. The weight of the one cubic centimeter sample was measured using a balance with one milligram accuracy. It was found that the densities of the blue, green and red fluorescent silica microfluid samples were 4.995×10^{-2}, 4.93×10^{-2} and 4.95×10^{-2} grams per cubic centimeter, respectively.

2.4.2 Experimental method used in the fractured greywacke injections

The silicon dioxide nanoparticles and fluorescent silica microspheres were injected to investigate their flow through the fractured greywacke core sample. The testing apparatus was similar to the permeability measurement experiment, but modified slightly to allow for the injection of nanoparticles. The configuration also allows for injection of particle-free deionized water, without interrupting the flow. The modified apparatus can be seen in Figure 2.2.

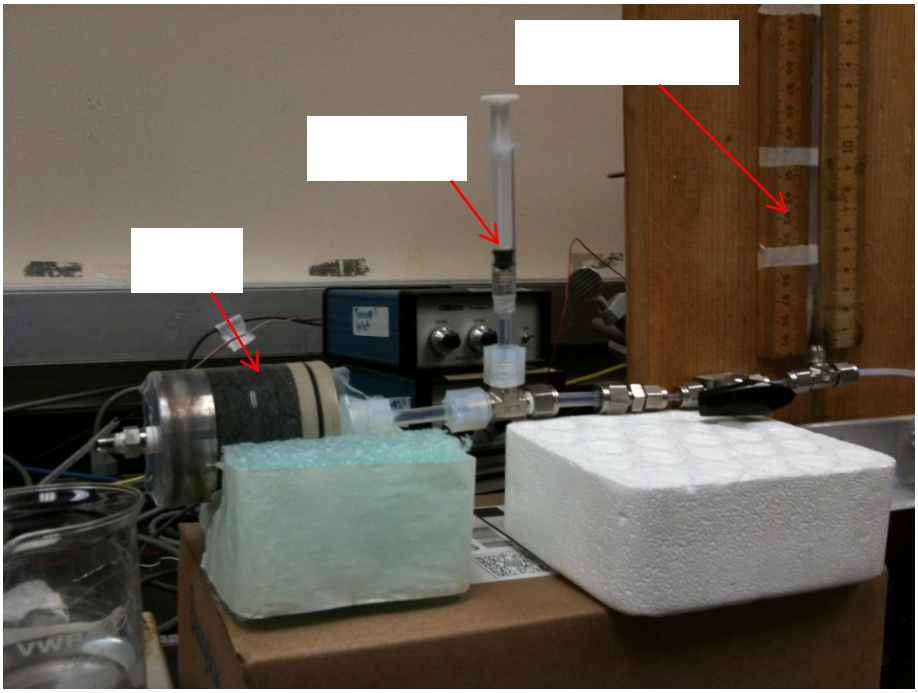

Figure 2.2: A picture of the silicon dioxide nanoparticle injection apparatus.

The nanofluid was contained in a syringe downstream the water pump. The nanoparticles were injected using the syringe. The silicon dioxide nanoparticle sample of unknown concentration was diluted one part to 50 parts of deionized water. The silica microsphere influent samples of two concentrations, one part to 50 and 100 parts of deionized water, were prepared, resulting in six influent samples (two blue, two green and two red samples). The new concentrations of the diluted samples are summarized in Table 1. The volume injected into the core sample was one cubic centimeter. Prior to the injection of the nanofluid, the core was preflushed with several pore volumes of water to displace rock fines and debris. Following the injection of the nanoparticles or microspheres (1 cm^3), a continuous flow of water was introduced. The core was then backflushed with several pore volumes to flush any trapped particles at the inlet side of the core. A total of 20 effluent samples including backflushing were collected and analyzed for each injection experiment (total of 120 samples).

Table 3.1: Summary of diluted samples concentration of blue, green and red fluorescent silica samples.

Sample	*Microfluid volume*	*Original concentration*	*Water volume*	*Diluted sample volume*	*Diluted sample concentration*
	cm^3	g/cm^3	cm^3	cm^3	g/cm^3
Blue silica spheres					
1 to 100	0.02	4.99×10^{-2}	1.98	2	4.99×10^{-4}
1 to 50	0.04	4.99×10^{-2}	1.96	2	9.99×10^{-4}
Green silica spheres					
1 to 100	0.02	4.93×10^{-2}	1.98	2	4.93×10^{-4}

1 to 50	0.04	4.93×10^{-2}	1.96	2	9.86×10^{-4}
Red silica spheres					
1 to 100	0.02	4.95×10^{-2}	1.98	2	4.95×10^{-4}
1 to 50	0.04	4.95×10^{-2}	1.96	2	9.90×10^{-44}

The sequence of the experiments was as follows. Initially, the silicon dioxide nanoparticles were injected and the core was then backflushed. The (1:100) diluted blue and green samples were then injected, followed by the injection of the (1:50) diluted blue and green samples. Effluent samples during injection and backflushing were collected following each injection. Due to the polydisperse nature of the red silica microspheres and concerns regarding plugging of the fracture by large spheres, both diluted samples of the red silica spheres (1:100 and 1:50) were injected last.

2.5 MAGNETIC COLLECTION EXPERIMENT

For nanosensors to provide information about the reservoir, they must be collected from the produced fluid. The use of paramagnetic nanoparticles may enable their collection from produced fluid using magnets. A preliminary experiment was performed to investigate the concept of magnetic collection of paramagnetic nanoparticles from flowing fluid. In order for a magnetic collection scheme to be successful, the magnetic force on the particles must dominate inertial, drag, gravitational, and diffusion forces acting on the particles (Moeser et al., 2004). In geothermal applications, it is likely that the two main competing forces will be the magnetic and inertial forces on the particles. Gerber and Birss (1983) define the magnetic force on a particle in a magnetic field as:

$$F_m = \mu_0 V_p M_p \bullet \nabla H \tag{2.1}$$

where F_m is the magnetic force, μ_0 is the constant permeability of free space, V_p is the volume of the paramagnetic particle, M_p is the magnetization of the particle, and ∇H is the magnetic field gradient. It is clear from Equation 2.1 that there are three parameters that can be tuned in order to increase the magnetic force on the particles: particle size, magnetization (which can be tuned by changing particle composition), and applied magnetic field gradient. It seems as if the applied magnetic field gradient may have the most potential as a tuning choice, because particle size and composition are constrained by other factors (e.g. mobility in the reservoir).

In this proof of concept experiment, it was decided to use low flow rates (i.e. low pressure gradient and inertial forces) in order to increase the likelihood of successful collection. The results of this experiment will be used to help design future experiments.

2.5.1 Experimental Methods

The experimental apparatus used for magnetic nanoparticle collection is illustrated in Figure 2.3.

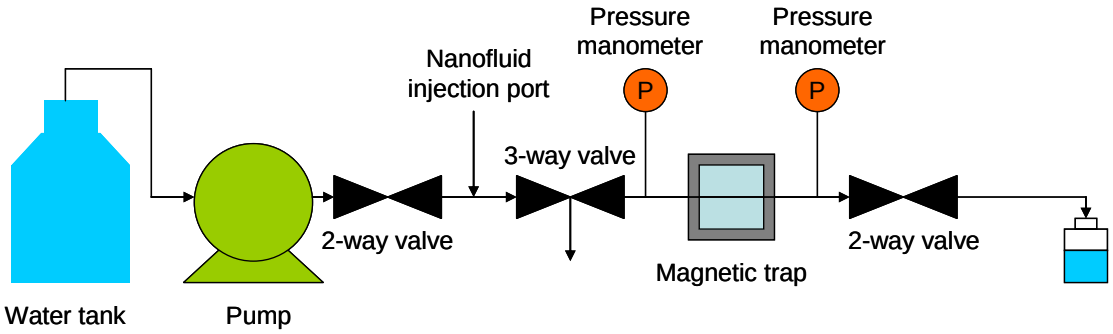

Figure 2.3: Schematic of experimental apparatus used in the magnetic collection experiment.

A Dynamax solvent delivery pump (Model SD-200) was used to pump water through the apparatus. Four BX084 neodymium block magnets manufactured by K&J Magnetics were used in the magnetic trap, with two magnets affixed to each side of the tube. This configuration was chosen in order to expose the injected nanoparticles to the strongest part of the magnetic field, which is illustrated in Figure 2.4. The proximity of the magnets is critical to the effectiveness of the collection scheme because magnetic force is a strong function of distance, as shown in Figure 2.5 for the particular magnets used.

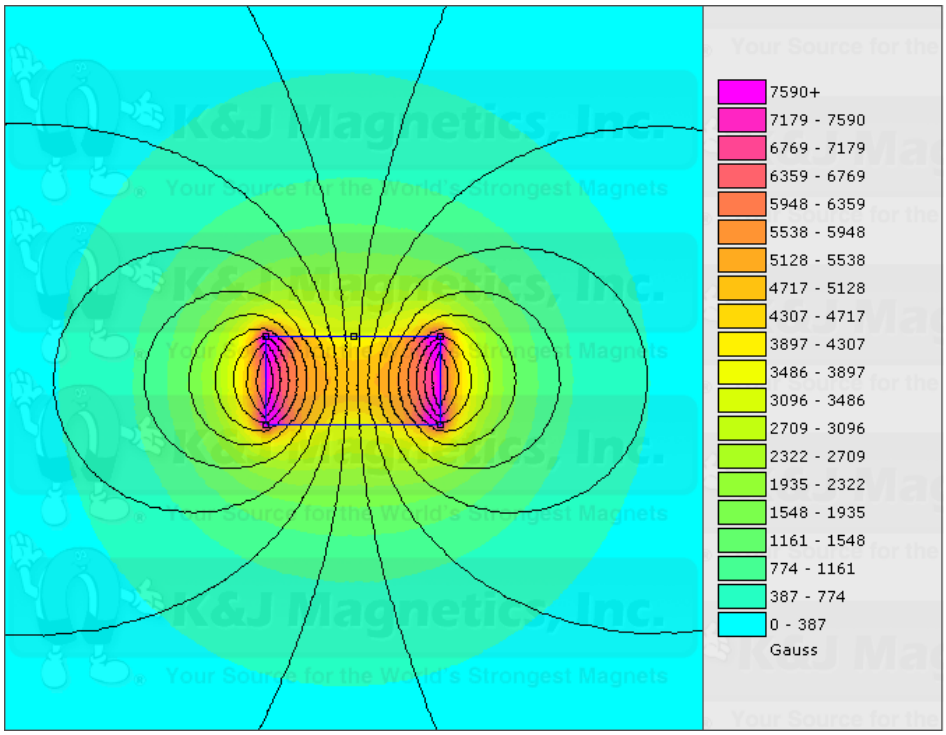

Figure 2.4: Magnetic field of neodymium block magnets. Reproduced from K&J Magnetics.

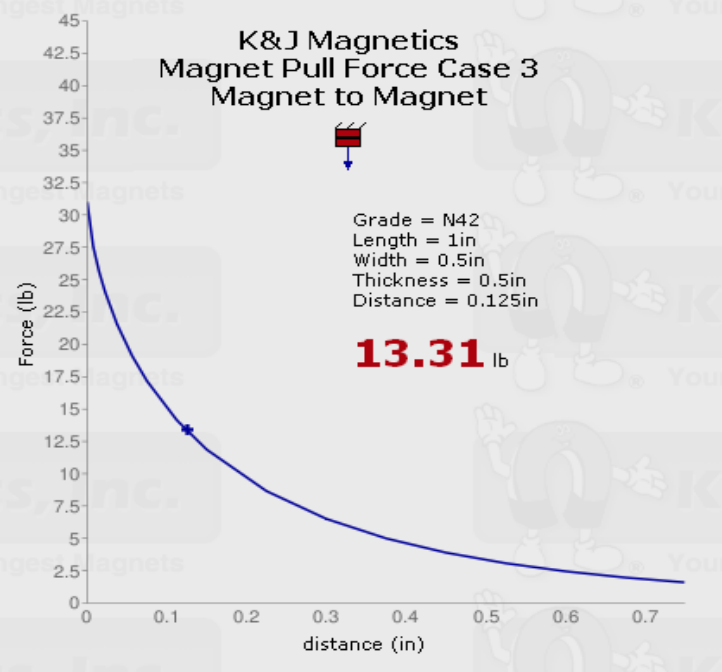

Figure 2.5: Magnetic pull force between two neodymium magnets as a function of distance. The point on the curve corresponds to 13.31 lb_f at a distance of 0.125 in., or the radius of the collection tube used. Reproduced from K&J Magnetics.

A 5 wt % suspension of paramagnetic iron oxide nanoparticles coated with silica in water were purchased from Corpuscular, Inc. These particles were characterized using SEM imaging, as shown in Figure 2.6.

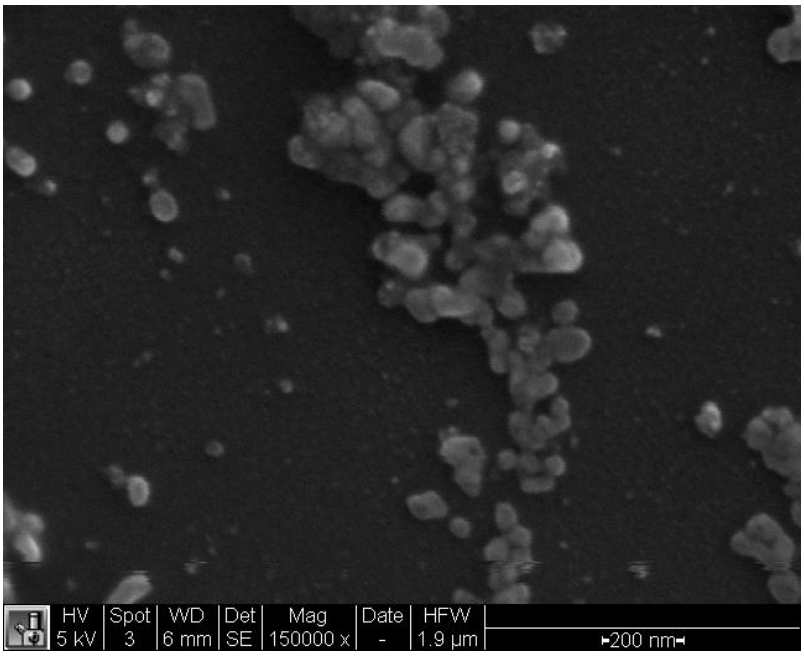

Figure 2.6: SEM image of iron oxide nanoparticles coated with silica.

The pump was used to fill the apparatus with water, the first valve was closed, the three-way valve was turned to allow water to be flushed out, and 1 ml of iron oxide nanofluid was injected. The valves were turned to their initial settings, water was pumped through the apparatus at a flow rate of 0.1 ml/min for 6.5 hours to push the nanofluid through the magnetic trap. All effluent was collected. Pressure remained constant throughout the experiment at 0.023 psig and 0.018 psig at the inlet and outlet of the collection tube, respectively. Most of the nanofluid was observed visually passing through the magnetic trap without being trapped. After flushing the apparatus with about 39 ml of water, the effluent was very dilute, and a small static cloud of nanofluid was observed at the outlet of the magnetic trap.

At this point, the flow rate was increased to 2.0 ml/min, and tendrils of previously static nanofluid were observed exiting the magnetic trap. The apparatus was flushed at this flow rate for about 50 min, at which point the effluent was visually indistinguishable from water. The pump was turned off, the valves were closed, and the magnetic trap was removed, revealing a cloud of nanoparticles that had been trapped by the magnets, as shown in Figure 2.7.

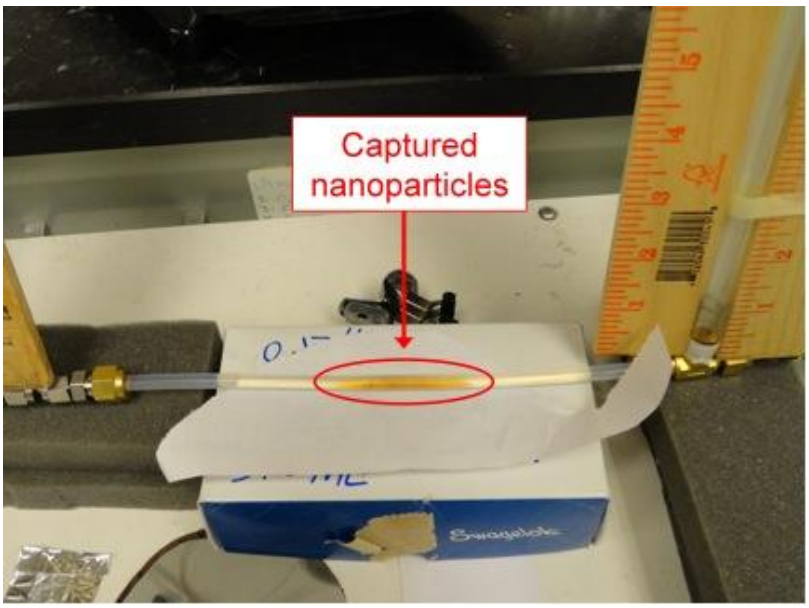

Figure 2.7: Photograph of trapped nanoparticles after the removal of the magnetic trap.

The outlet side of the collection tube was disconnected, and the previously trapped nanoparticles were collected. The volume of the collected fluid was measured to be 3.7 ml. In order to calculate collection efficiency, the concentration of the nanoparticles in the trapped sample had to be estimated. This was done by using UV-vis spectroscopy to measure the absorbance spectra of the trapped sample and of dilutions prepared from the original nanofluid with known concentrations. The absorbance at a specific wavelength was found to scale linearly with concentration, and the resulting correlation was used estimate the concentration of the collected sample. The baseline concentration of nanoparticles was calculated to be 0.08 g/ml using the 5 wt % specified by the manufacturers and the measured nanofluid density of 1.6 g/ml.

2.6 RESULTS

2.6.1 Fluorescent Silica Injection Results

This section provides the results of the injection of fluorescent silica microspheres into the fractured greywacke core. Prior to the injection of the silica spheres, silicon dioxide nanoparticles were injected. The objective of this experiment was to investigate the transport of silicon dioxide nanoparticles through fractured greywacke core, providing a baseline for subsequent injections of the fluorescent silica microspheres.

The silicon dioxide (SiO_2) nanoparticles flowed through the fractured greywacke core successfully. The results were discussed fully in the previous quarterly report (January-March, 2011)

The fluorescent silica microspheres were also transported through the fractured greywacke core successfully. As mentioned earlier, the silica microsphere influent samples of the same concentration (but different size) were injected consecutively. That is the injection of the blue silica microspheres diluted (1:100) was followed by the (1:100) diluted green silica microspheres. Following that, the blue silica microspheres influent with doubled concentration (1:50 dilution) was injected, followed by the green silica microspheres influent of the same concentration.

The silica microspheres were identified in the effluent samples using optical microscopy and fluorescence spectroscopy, confirming their delivery through the fracture. Examples of the optical imaging performed on collected effluent samples after the injection of the (1:100) diluted blue and (1:50) green silica microspheres can be seen in Figure 2.8. Similar images were obtained for effluents resulted from the other injections (i.e. the (1:50) blue and (1:100) green injections experiments).

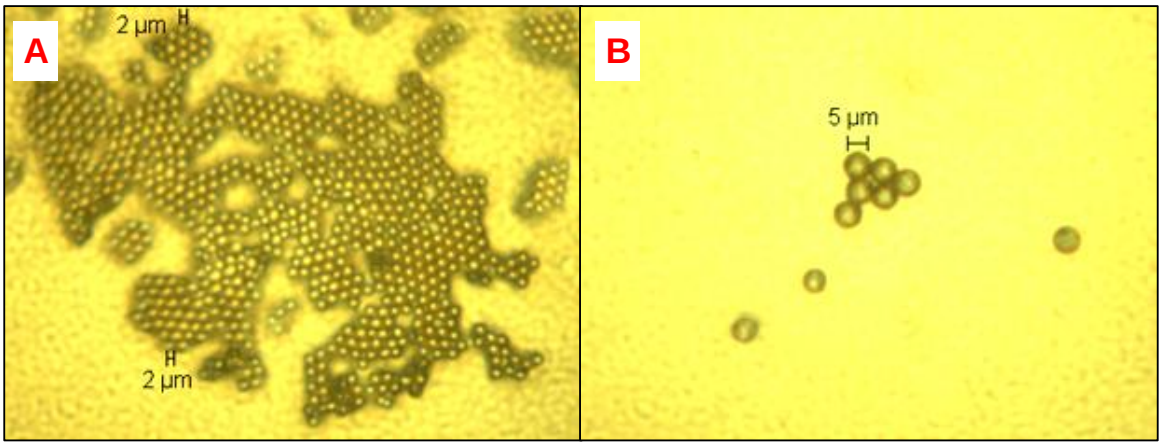

Figure 2.8: Optical images of the effluent during the (A) blue and (B) green silica microsphere injections.

The recovery of the silica microspheres was determined by measuring the emission spectrum and correlating it to the effluent concentration using a calibration curve. The

fluorescence emission spectra of all effluent and backflushing samples collected during the blue silica microsphere injection (1:100 and 1:50) are shown in Figure 2.9. The samples were excited at a wavelength of 350 *nm* and the emission spectrum was measured between 350 to 600 *nm*, with a peak or maximum emission at a wavelength of about 434 *nm*. To construct the calibration curve, the emission spectra of a few samples of known concentrations were acquired. The concentrations of effluent samples were determined based on the maximum emission intensity at the peak. The return curves of the blue microspheres were then estimated as depicted in Figure 2.10. It was found that about 54% of the injected (1:100) diluted blue spheres influent was recovered. The microspheres were produced throughout the post injection at roughly constant level ($\pm 1.5 \times 10^{-5}$ g/cm^3), with no clear or identifiable peak. On the other hand, only 19% of the (1:50) blue spheres influent was recovered, mostly during the post injection of the first five pore volumes. Note that this injection followed the injection of the (1:100) green spheres. The green silica spheres were more than twice the size of the blue spheres. It was hypothesized that part of the fracture might have been plugged causing the microparticles to accumulate at plugged sections and hence cause entrapment of subsequently injected spheres (i.e. 1:50 blue spheres).

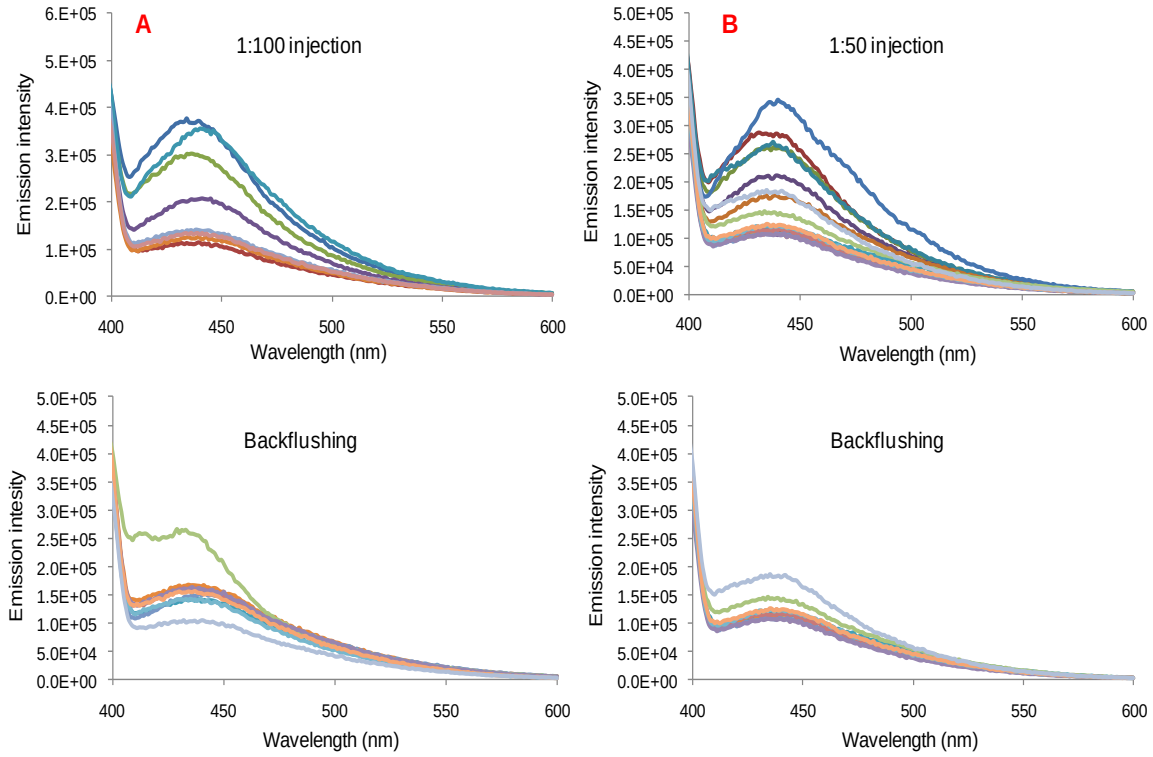

Figure 2.9: Emission spectra of effluent and backflushing samples during (A) 1:100 and (B) 1:50 dilutions of the blue silica spheres.

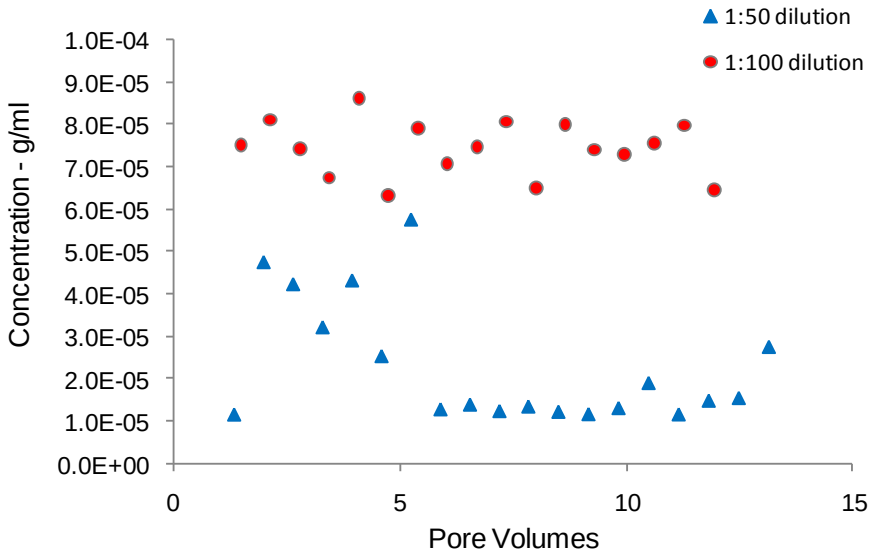

Figure 2.10: Blue silica microspheres return curves.

To support this finding, we attempted to estimate the recovery of the green silica microspheres. The (1:100) and (1:50) green spheres influents followed the injection of the (1:100) and (1:50) blue spheres samples. The construction of the calibration curve of the green silica microspheres was not feasible due to discrepancies in the fluorescence emission spectra measurements of diluted samples. However, we attempted to estimate the average recovery of the green spheres by calculating the cumulative ratio of emission intensity of effluent (E_e) to emission intensity of influent (E_i). The fluorescence emission spectra of effluent and backflushing samples of the green silica microsphere injection (1:100 and 1:50) are shown in Figure 2.11. The effluent and backflushing samples were excited at wavelength 480 *nm* and the emission spectrum was acquired between 480 to 700 *nm*, with maximum emission at wavelength of about 525 *nm*.

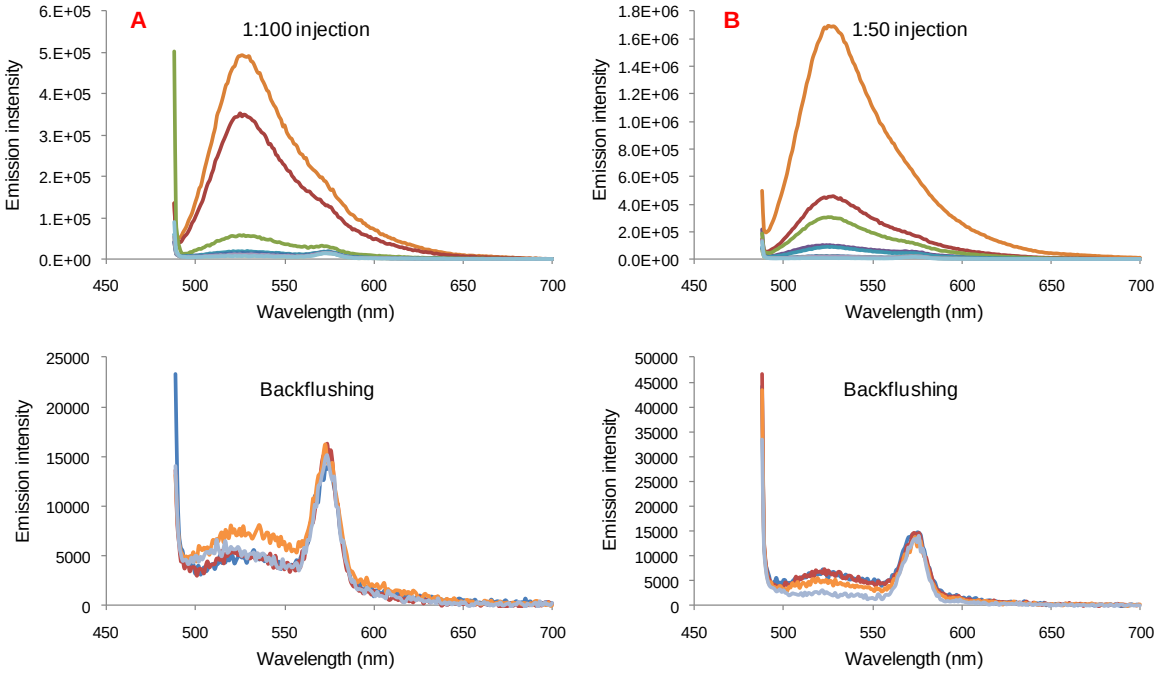

Figure 2.11: Emission spectra of effluent and backflushing samples during (A) 1:100 and (B) 1:50 dilutions of the green silica spheres.

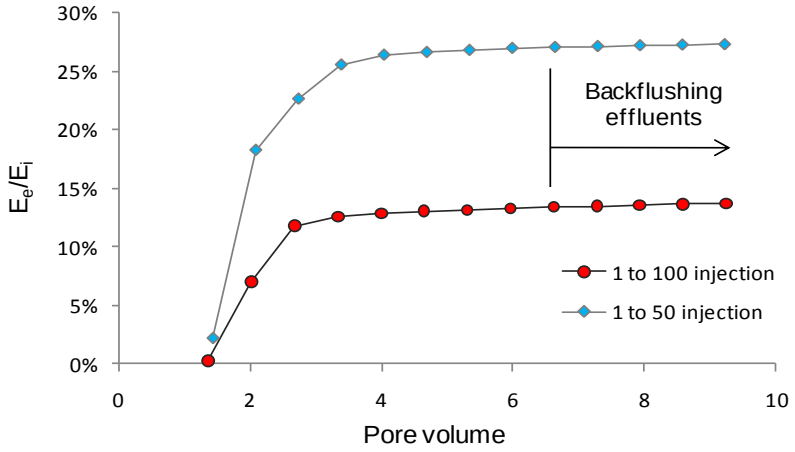

Figure 2.12: Green silica spheres cumulative ratio of emission intensity of effluent (E_e) to influent (E_i) as function of pore volumes injection.

Figure 2.12 shows the cumulative ratio of emission intensity of effluent to that of the influent. In the case of the 1:100 green spheres injection, the cumulative emission intensity ratio reached a plateau at around 13.7%, indicating a poor recovery of the microspheres. Many spheres were trapped within the fractured core. This injection preceded the (1:50) blue spheres injection. The plugging of the green spheres may have resulted in the poor recovery (19%) during the injection of the (1:50) blue spheres. In the case of the 1:50 green sphere injection, the recovery of particles was about 27.3%, double the value observed in the 1:100 injection.

We have demonstrated the feasibility of transporting nanoparticles and/or microparticles through a fractured geothermal greywacke core. In terms of characterizing the fractures in the rock, which is a primary objective of the project, the preliminary experiments showed promise. Figure 2.13 is an SEM image from within the pore spaces of Berea sandstone following the injection of silicon dioxide (SiO_2) nanoparticles. This shows that the nanoparticles passed through pores of sizes larger than themselves, but were unable to pass into the tinier natural fracture that existed within the rock structure. A smaller nanoparticle could have entered the fracture providing a direct correlation between the recovered particle size and fracture aperture. Therefore, it may be possible to use nanoparticles as a form of fracture aperture caliper.

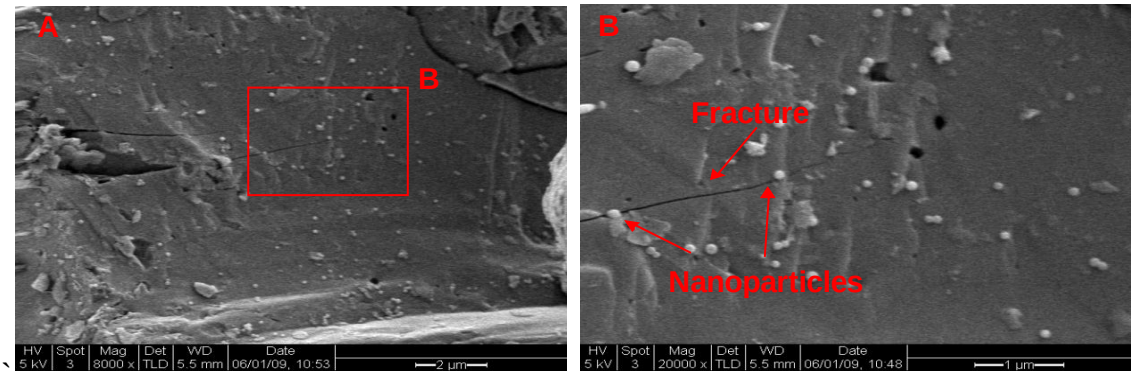

Figure 2.13: (A) Natural fracture with two nanoparticles at its entry, (B) close-up image. Smaller nanoparticles would enter the fracture providing direct fracture aperture measurement based on recovered particle size.

Investigation into the idea of using particles to measure the fracture aperture was carried out by injecting the polydisperse (diameter ranging from 5 to 31 μm) red silica microsphere influent (Figure 2.14A) into the fractured greywacke core. It was found that only microspheres with diameters smaller than 20 μm were transported through the fracture (Figure 2.14B). This suggested that the fracture has an aperture of at least 20 μm, but not as large as 31 μm. This result was in agreement with the hydraulic fracture aperture measurement (i.e. 27 μm as determined from the cubic law), and demonstrates the possibility of using particles to estimate the size of the fracture opening. Another interesting finding was that the particle size did not need to be three times smaller than the space available for its flow (the rule of thumb commonly used to size membrane filters).

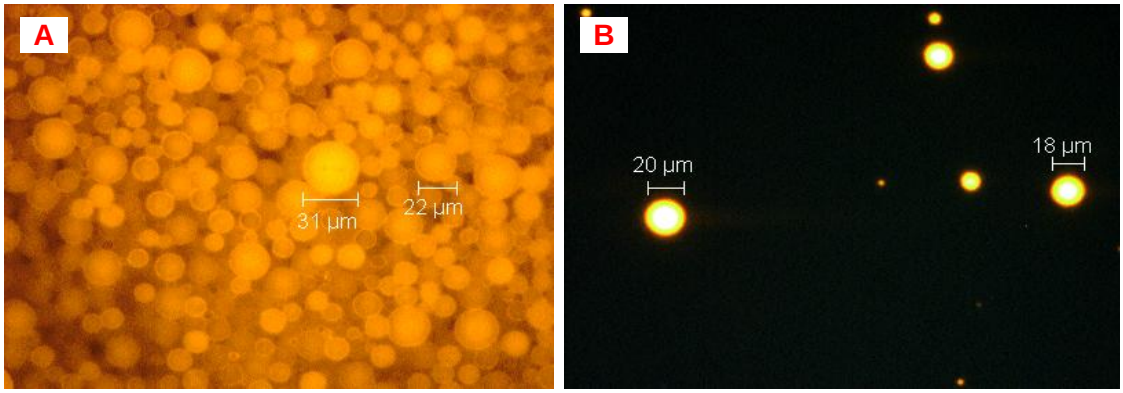

Figure 2.14: Optical images for red fluorescent silica microspheres of (A) influent, (B) effluent samples. Only spheres of about 20 µm *flowed through the fracture of predetermined aperture of 27* µm.

The recovery of the red silica microspheres was determined by calculating the ratio of fluorescence emission intensity of effluent to that of the influent. Two diluted influent samples (1:100) and (1:50) of red spheres were injected one after the other. Note that the fractured core was flushed with many pore volumes prior to the injection of the red spheres; in attempt to mobilize and remove any remaining microspheres from previous injections (blue and green silica spheres). The core was also dried and resaturated again. The cumulative emission intensity ratio as a function of pore volumes injected is shown in Figure 2.15. The recovery following the (1:100) influent injection was around 15.7%. Acquiring the emission spectrum of some effluent and backflushing samples was not possible, because fluorescence levels in these samples were below detection limit of the instrument. The recovery was improved to 47.5% when the concentration of influent was doubled (i.e. 1:50 dilution).

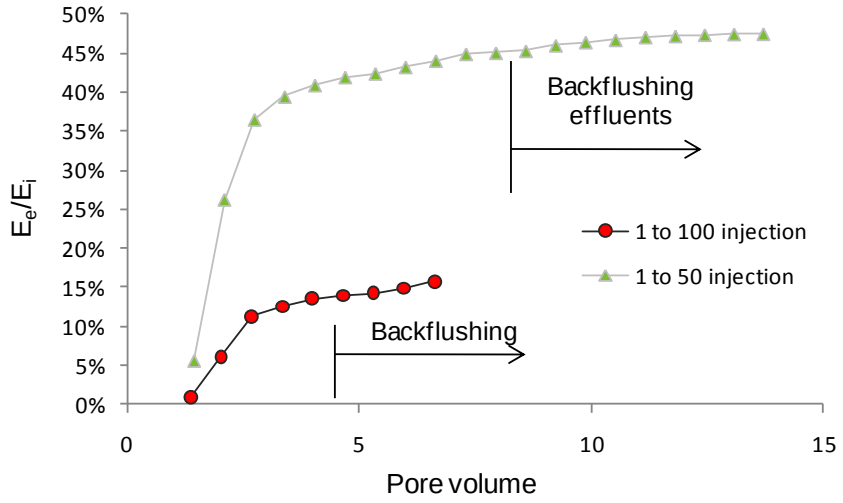

Figure 2.15: Red silica spheres cumulative ratio of emission intensity of effluent (E_e) to influent (E_i) as function of pore volumes injection.

2.6.2 Magnetic Collection Experimental Results

In order to calculate the collection efficiency, or the percentage of injected nanoparticles that were retained in the magnetic trap at the end of the experiment, dilutions of the original nanofluid with known concentrations were prepared. The dilution with the closest visual match to the trapped nanofluid is shown in Figure 2.16.

Figure 2.16: Visual comparison of trapped nanofluid sample and 142.5 to 1 dilution of original nanofluid.

The absorbance spectra of the trapped nanofluid and the prepared dilutions were measured using UV-vis spectroscopy, and are shown in Figure 2.17. As is predicted by Beer's Law, concentration was found to scale linearly with absorbance. This is shown in Figure 3-8. For this correlation, the absorbance was read at a wavelength of 460 nm, because the spectra have an inflection point at this wavelength.

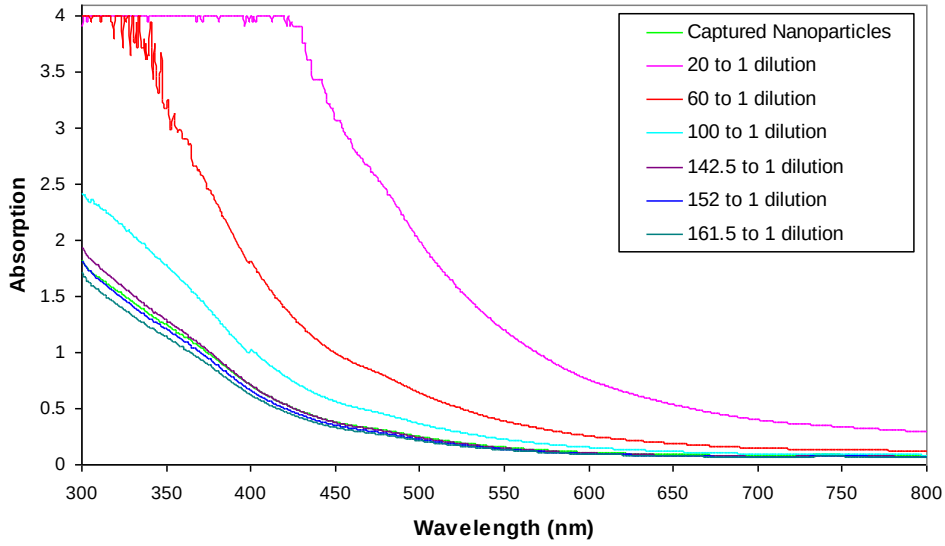

Figure 2-17: Absorbance spectra of suspensions of iron oxide nanoparticles coated with silica.

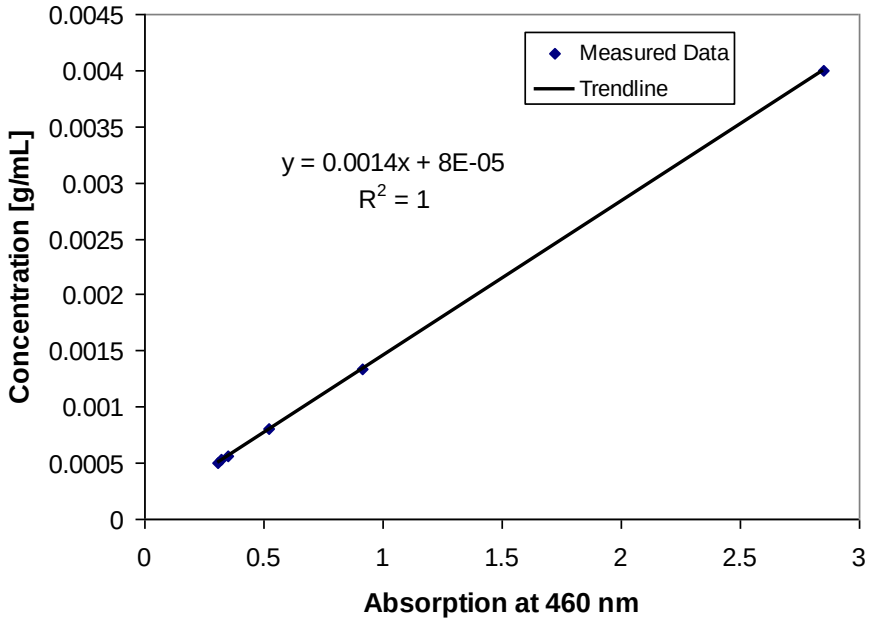

Figure 2-18: Correlation of concentration to absorbance for dilutions of iron oxide nanofluid with known concentrations.

Using the correlation shown in Figure 2-18, the concentration of the trapped nanofluid was estimated to be 0.00057 g/ml. The collection efficiency was calculated using Equation 2.2.

$$\eta_{collection} = \frac{m_{collected}}{m_{injected}} * 100\% = \frac{C_{collected} V_{collected}}{C_{injected} V_{injected}} * 100\% \qquad (2.2)$$

where $\eta_{collection}$ is collection efficiency, m denotes mass, C denotes concentration, and V denotes volume. The collection efficiency for this experiment was estimated to be 3%.

2.7 FUTURE WORK

It is planned to continue our investigation of the flow of particles through fractured core rocks. Several core samples will be saw-cut to create fractures of predetermined aperture.

Further magnetic collection experiments will also be performed using different magnets and configurations in order to increase collection efficiency.

3. FRACTURE CHARACTERIZATION USING RESISTIVITY

This research project is being conducted by Research Assistant Lilja Magnusdottir, Senior Research Engineer Kewen Li and Professor Roland Horne. The objective of this project is to investigate ways to use resistivity to infer fracture properties in geothermal reservoirs.

3.1 SUMMARY

The aim of this project is to use resistivity measurements and modeling to characterize fracture properties in geothermal fields, both natural and EGS. The resistivity distribution of a field can be estimated by measuring potential differences between various points while injecting an electric current into the ground and resistivity data can be used to infer fracture properties due to the large contrast in resistivity between water and rock. The contrast between rock and fractures can be increased further by injecting a conductive tracer into the reservoir thereby decreasing the resistivity of the fractures. In this project, the potential difference has been calculated between two points (an injector and a producer) as conductive fluid flows through fracture networks. The time history of the potential field depends on the fracture network and can therefore be used to estimate where fractures are located and the character of their distribution.

The analogy between Ohm's law that describes electrical flow and Darcy's law describing fluid flow makes it possible to use flow simulator TOUGH2 to calculate electric fields. This report discusses how TOUGH2 was used first to solve the flow of a conductive fluid through three different fracture networks and then used to calculate the electric potentials of the fields for each time step in order to obtain the time history of the potential difference between the injector and the producer as the conductive fluid flows through the fractures. By using TOUGH2 to solve the electric field instead of previously used resistivity model described in preceding quarterly report (Jan-March 2011), the same grid can be used for both electric and fluid flow models. TOUGH2 also allows the use of nonrectangular elements, making the simulation faster and more efficient.

Future work includes studying further the relationship between fracture networks and the change in potential differences as conductive tracer is injected into the reservoir for more complicated fractal network of fractures. Another future goal is to study the possibility of using the potential differences with inverse modeling to characterize fracture patterns. It is also of interest to study different electrode layouts and the minimum number of wells needed for this inverse modeling method to characterize the fractures sufficiently as well as to explore the use of nanotracers (see Section 2) and the influence of injecting varying tracer concentrations.

3.2 INTRODUCTION

Characterizing the dimensions and topology of fractures in geothermal reservoirs is crucial for optimal designing of production and to find feasible drilling locations. Fractures carry most of the fluid in the reservoir so fracture configuration is central to the performance of a geothermal system both in fractured reservoirs as well as in Enhanced Geothermal System (EGS) applications. The knowledge of fluid-flow patterns is necessary to ensure adequate supply of geothermal fluids and efficient operation of geothermal wells and to prevent

short-circuiting flow paths from injector to producer that would lead to premature thermal breakthrough. Fracture characterization therefore increases the reliability of geothermal wells and the overall productivity of geothermal power plants.

The goal of this study is to find ways to use Electrical Resistivity Tomography (ERT) to characterize fractures in geothermal reservoirs. ERT is a technique for imaging the resistivity of the subsurface from electrical measurements. Pritchett (2004) concluded based on a theoretical study that hidden geothermal resources can be explored by electrical resistivity surveys because geothermal reservoirs are usually characterized by substantially reduced electrical resistivity relative to their surroundings. Electrical current moving through the reservoir passes mainly through fluid-filled fractures and pore spaces because the rock itself is normally a good insulator. In these surveys, a direct current is sent into the ground through electrodes and the voltage differences between them are recorded. The input current and measured voltage difference give information about the subsurface resistivity, which can then be used to infer fracture locations.

Resistivity measurements have been used in the medical industry to image the internal conductivity of the human body, for example to monitor epilepsy, strokes and lung functions as discussed by Holder (2004). In Iceland, ERT methods have been used to map geothermal reservoirs. Arnarson (2001) describes how different resistivity measurements have been used effectively to locate high temperature fields by using electrodes located on the ground's surface. Stacey et al. (2006) investigated the feasibility of using resistivity to measure saturation in a rock core. A direct current pulse was applied through electrodes attached in rings around a sandstone core and it resulted in data that could be used to infer the resistivity distribution and thereby the saturation distribution in the core. It was also concluded by Wang and Horne (2000) that resistivity data have high resolution power in the depth direction and are capable of sensing the areal heterogeneity.

In the approach considered in this project so far, electrodes would be placed inside two geothermal wells (future work will involve studying different electrode arrangements with a greater number of wells) and the potential differences between them studied to locate fractures and infer their properties. Due to the limited number of measurement points, the study is investigating ways to enhance the process of characterizing fractures from sparse resistivity data. For example, in order to enhance the contrast in resistivity between the rock and fracture zones, a conductive tracer could be injected into the reservoir and the time-dependent voltage difference measured as the tracer distributes through the fracture network.

Slater et al. (2000) have shown a possible way of using Electrical Resistivity Tomography (ERT) with a tracer injection by observing tracer migration through a sand/clay sequence in an experimental $10 \times 10 \times 3$ m^3 tank with cross-borehole electrical imaging. Singha and Gorelick (2005) also used cross-well electrical imaging to monitor migration of a saline tracer in a $10 \times 14 \times 35$ m^3 tank. In previous work, usually many electrodes were used to obtain the resistivity distribution for the whole field at each time step. The resistivity distribution was then compared to the background distribution (without any tracer) to see

resistivity changes in each block visually, to locate the saline tracer and thereby the fractures. Using this method for a whole reservoir would require a gigantic parameter space, and the inverse problem would not likely be solvable, except at very low resolution. However, in the method considered in this study, the potential difference between the wells would be measured and plotted as a function of time while the conductive tracer flows through the fracture network. Future work will involve using that response, i.e. potential difference vs. time, in an inverse modeling process to characterize the fracture pattern.

In this report, first, the analogy between water flow and electrical flow is defined. Then, the flow of conductive fluid through three different fracture networks is calculated using TOUGH2 flow simulator and the electric field is solved for each time step as the fluid flows through the fractures. The results for the time history of the potential difference between the injector and the producer are described. Finally, future work is outlined.

3.3 WATER FLOW ANALOGY OF ELECTRICAL FLOW

The steady-state flow of an electric current through a conducting medium due to differences in energy potential is analogous to the steady-state flow of a fluid through porous medium. Darcy's law is an empirical relationship similar to Ohm's law,

$$J = -\sigma \nabla \phi \tag{3.1}$$

where J is current density [A/m^2], σ is the conductivity of the medium [Ωm] and ϕ is the electric potential [V] but instead of describing electrical flow Darcy's law describes fluid flow through a porous medium,

$$q = -\frac{k}{\mu} \nabla p \tag{3.2}$$

where q is the flow rate [m/s], k is permeability [m^2], μ is viscosity of the fluid [kg/ms] and p is pressure [Pa]. Table 1 presents the correspondence between the variables and relations of water flow (Darcy's law) and electric current flow (Ohm's law).

Table 1: Correspondence between electric current flow and water flow.

	Darcy's law: $q = -\frac{k}{\mu} \nabla p$	Ohm's law: $J = -\sigma \nabla \phi$
Flux of:	Water q [m/s]	Charge J [A/m^2]
Potential:	Pressure p [Pa]	Voltage ϕ [V]
Medium property:	Hydraulic conductivity $\frac{k}{\mu}$ [m^2/Pa·s]	Electrical conductivity σ [1/Ωm]

The similarities between these two equations imply that it is possible to use flow simulator like TOUGH2 to solve for the electric field due to flow of electric current. Then, the pressure results from TOUGH2 correspond to the electric voltage, the current density to

the flow of water and the electrical conductivity would correspond to the hydraulic conductivity, i.e.

$$\sigma = \frac{k}{\mu} \tag{3.3}$$

3.4 RESULTS

A flow simulation was performed using the TOUGH2 reservoir simulator to see how a tracer, which increases the conductivity of the fluid, distributes after being injected into the reservoir. The simulation was carried out on a two-dimensional grid with dimensions 1000 × 1000 × 10 m^3 with fractures first modeled as a cross in the upper left corner (green blocks) as shown in Figure 3.1, then as a larger cross in the upper left corner as Figure 3.2 shows and finally with no fractures.

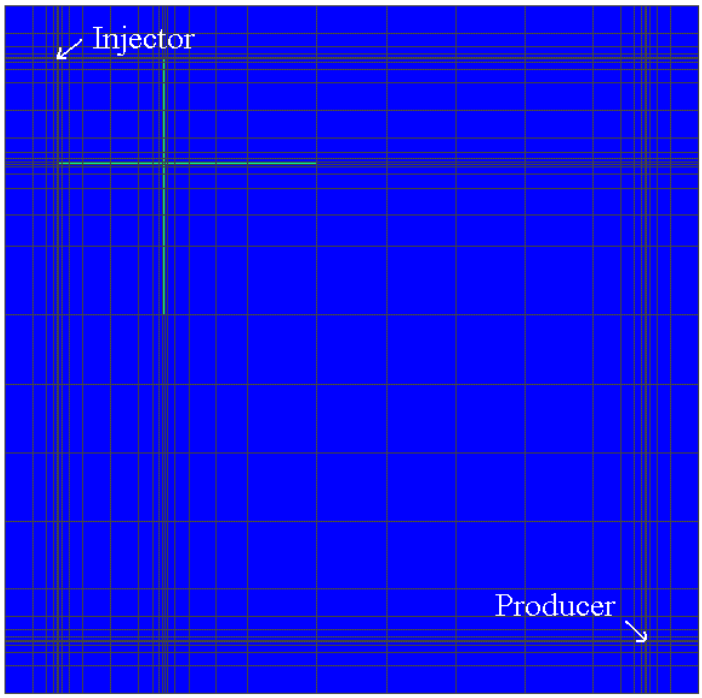

Figure 3.1: Fractures (green blocks) modeled as a small cross in the upper left corner of the reservoir.

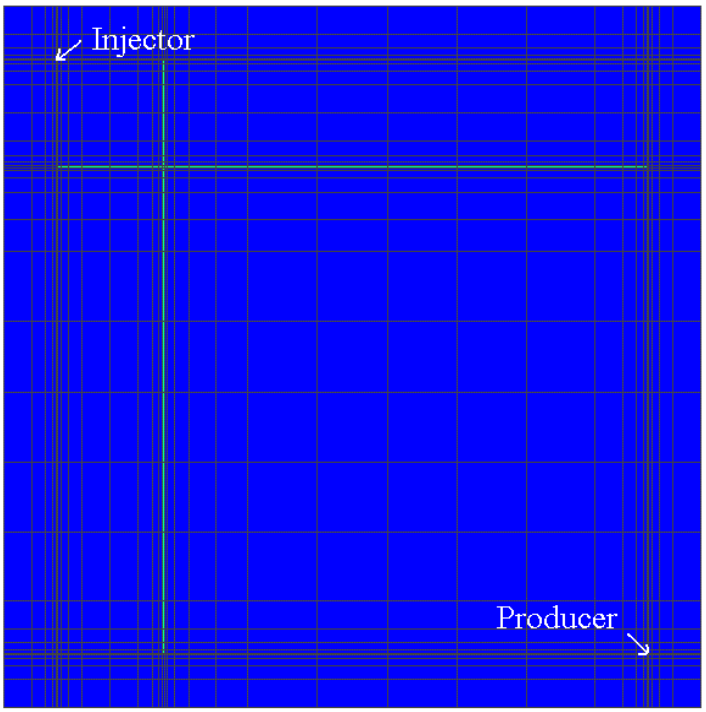

Figure 3.2: Fractures (green blocks) modeled as a larger cross in the upper left corner of the reservoir.

The goal was to study the difference in potential field between these three cases as conductive fluid is injected into the reservoir. The reservoir is modeled with porosity 0.2 and permeability 10^5 md (10^{-10} m^2) while the fractures have permeability 5×10^9 md (5×10^{-4} m^2). No-flow boundary conditions were used and 100 kg/s of water was injected in the upper left corner with enthalpy 100 kJ/kg, and 0.1 kg/s of tracer with enthalpy 100 kJ/kg. The initial pressure was set to 10 atm, temperature to 150°C and initial tracer mass fraction to 10^{-9} because the simulator could not solve the problem with zero initial tracer mass fraction.

The tracer injected into the reservoir is a NaCl solution whose resistivity changes with temperature and concentration. Ucok et al. (1980) have established experimentally the resistivity of saline fluids over the temperature range 20-350°C and their results for resistivity of NaCl solution calculated using a three-dimensional regression formula is shown in Figure 3.3.

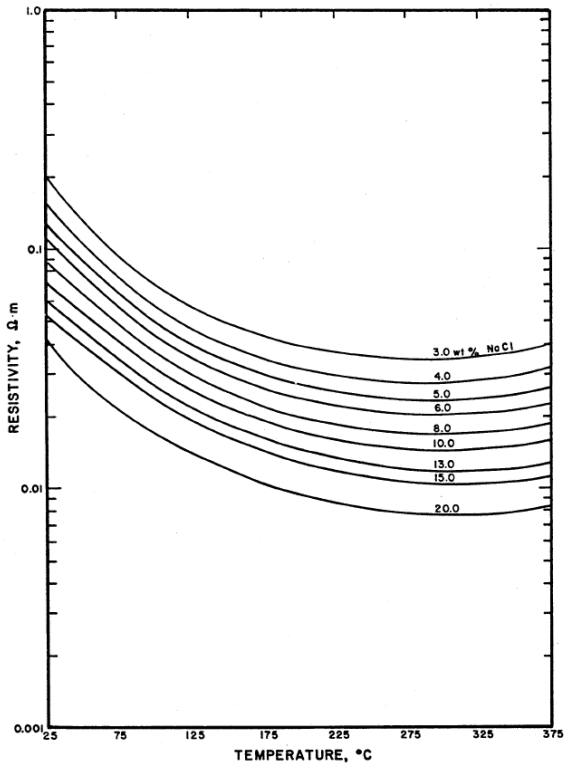

Figure 3.3: Resistivity of NaCl solution as a function of temperature and concentration (from Ucok et al., 1980).

Ucok et al. (1980) calculated that the dependence of resistivity is best represented by the formula:

$$\rho_w = b_0 + b_1 T^{-1} + b_2 T + b_3 T^2 + b_4 T^3 \tag{3.4}$$

where T is temperature and b are coefficients found empirically. The best fit for the concentration dependence was found to be:

$$\rho_w = 10/(\Lambda c) \tag{3.5}$$

where

$$\Lambda = B_0 - B_1 c^{1/2} + B_2 c \ln c + higher\ order\ terms \tag{3.6}$$

Coefficients B depend on the solution chemistry and c is the molar concentration.

In this project, the tracer concentration resulting from the flow simulation was changed into molar concentration and the following B coefficient matrix for the three-dimensional regression analysis of the data studied by Ucok et al. (1980) was used to calculate the resistivity of the NaCl solution,

$$B = \begin{matrix} 3.470 & -6.650 & 2.633 \\ -59.23 & 198.1 & -64.80 \\ 0.4551 & -0.2058 & 0.005799 \\ -0.346E\text{-}5 & 7.368E\text{-}5 & 6.741E\text{-}5 \\ -1.766E\text{-}6 & 8.787E\text{-}7 & -2.136E\text{-}7 \end{matrix}$$

Therefore, the resistivity value of each block depends on the tracer concentration in that block and the value decreases as more tracer flows into the block.

The TOUGH2 flow simulator was used to calculate the electric potential distribution for the reservoirs. A current is set equal to 1 A at a point in the upper left corner, and as -1 A at the lower right corner and the potential field calculated based on the resistivity of the field at each time step. Figures 3.4 and 3.5 show how the potential difference between the injector and the producer changes with time for the reservoirs shown in Figure 3.1 and 3.2 and Figure 3.6 shows the potential difference time history for the reservoir with no fractures.

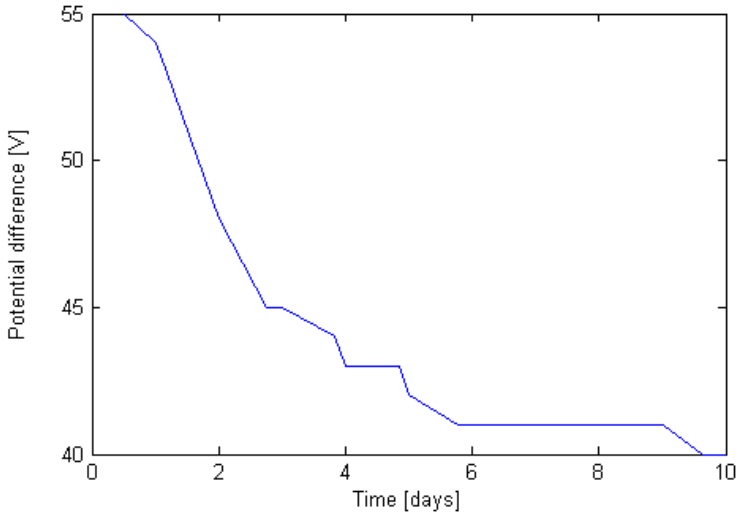

Figure 3.4: Potential difference between injection and production wells for reservoir in Figure 3.1.

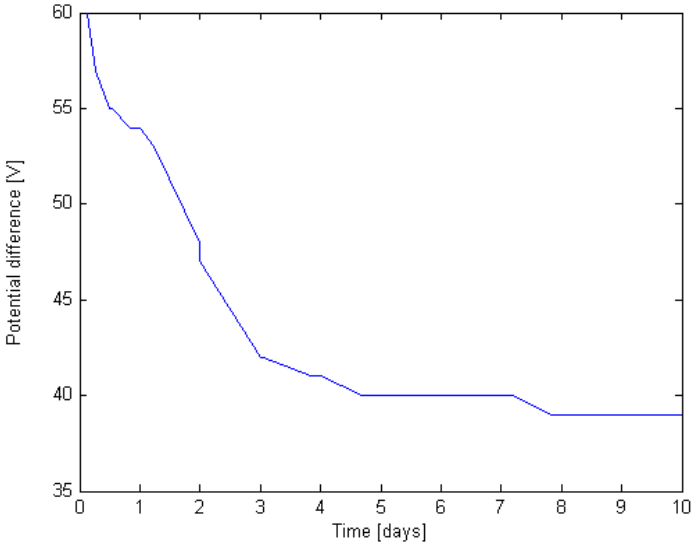

Figure 3.5: Potential difference between injection and production wells for reservoir in Figure 3.2.

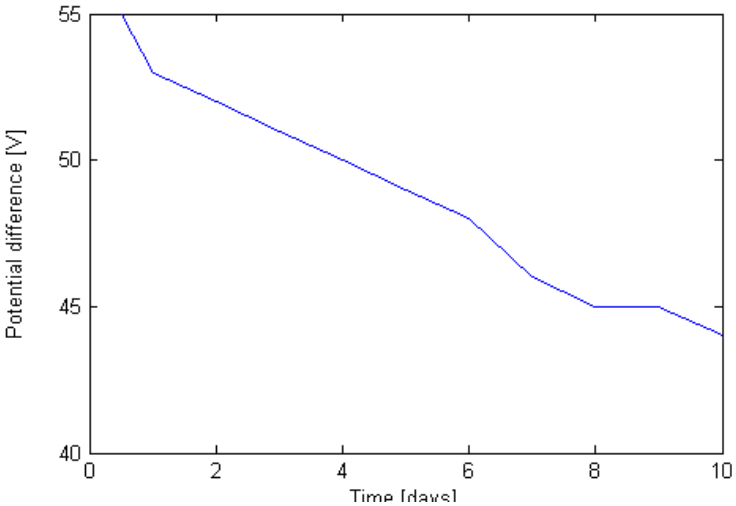

Figure 3.6: Potential difference between injection and production wells for the reservoir with no fractures.

The potential difference in the graph in Figure 3.5 drops faster than the difference in Figure 3.4 because of larger fractures enabling conductive fluid to flow faster through the reservoir. Figure 3.6 shows a much slower decline in potential difference because the reservoir has no fractures. The potential difference after 10 days of injection is 39 V for the larger fractured reservoir, 40 V for the smaller fractured reservoir and 44 V for the reservoir with no fractures. The results also indicate that different fracture properties give different potential difference histories between two wells, and could therefore be used to indicate fracture characteristics.

The results also showed how TOUGH2 flow simulator could be used to solve both tracer flow and electric potential for fracture networks. By using TOUGH2 and the same grid for both simulations, nonrectangular elements could be used, making the simulation faster and more efficient.

3.5 FUTURE WORK

Future work will include looking at more complicated and realistic fracture networks to study further the relationship between fracture networks and the change in potential differences as conductive tracer is injected into the reservoir. It is also of interest to study the use of nanotracers as well as to explore the influence of injecting varying conductive tracer concentration.

Other future goals are to use tracer concentration simulations and electrical potential calculations from TOUGH2 with inverse modeling to estimate the dimensions and topology of a fracture network. The objective is to develop a method that can be used to find where fractures are located and the character of their distribution.

In inverse modeling the results of actual observations are used to infer the values of the parameters characterizing the system under investigation. In this study, the output

parameters would be the potential differences between wells as a function of time and the input parameters would include the dimensions and orientations of the fractures between the wells. The objective function measures the difference between the model calculation (the calculated voltage difference between the wells) and the observed data (measured potential field between actual wells), as illustrated in Figure 3.7, and a minimization algorithm proposes new parameter sets that improve the match iteratively.

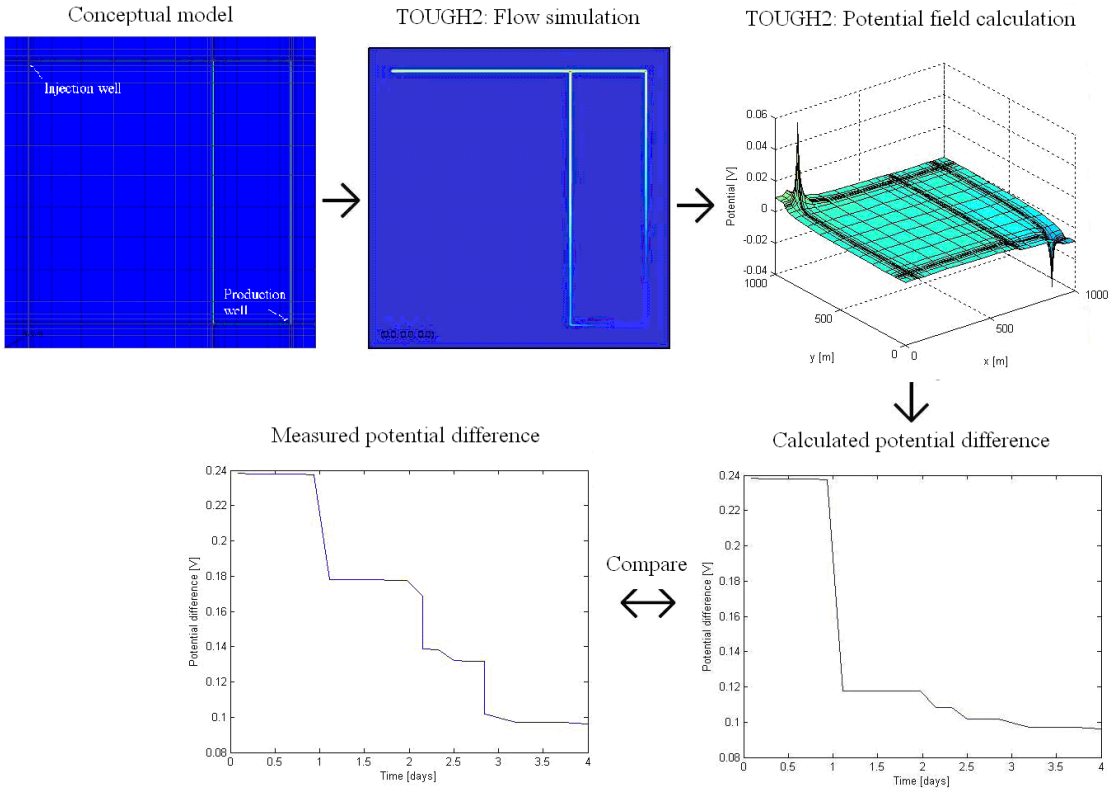

Figure 3.7: The inverse problem; the calculated potential difference is compared to the measured potential difference and the inverse problem solved to characterize fracture patterns.

The possibility of using fewer wells and different well arrangements will be studied to estimate the minimum number of measurement locations necessary to solve the problem.

4. FRACTURE APERTURE DETERMINATION USING THERMAL AND TRACER DATA

This research project is being conducted by Research Associate Carla Kathryn Co and Professor Roland Horne. The overall objective of this study is to develop a methodology to estimate fracture dimensions in geothermal rocks. Our current focus is on utilizing thermal breakthrough and tracer return data to determine effective fracture aperture.

4.1 SUMMARY

This study aimed to determine an effective fracture aperture using tracer concentration and thermal breakthrough profiles. A single fracture was used to represent the connectivity between injection and production well pairs. An analytical model derived by Gringarten and Sauty (1975) was used to estimate the fracture aperture from thermal breakthrough time and mean tracer arrival time. Estimated effective fracture aperture values were recalculated and now vary from 2.1 cm to 42.6 cm.

A literature review was undertaken to seek field data. In fields Desert Peak, Nevada and Wairakei, New Zealand, fracture properties were determined from acoustic imaging techniques. Feed zone locations identified through pressure, temperature, and spinner (PTS) data were then correlated to these properties. Results showed that feed zone locations correspond to depths with higher apertures. Fracture density, however, was not found to be relevant to fluid entry zones.

Comparison of cooling rate predictions from three interwell connection models was done this quarter using data from Palinpinon geothermal field (Maturgo et al, 2010). These models were: single fracture model; porous model with heat loss; and isotropic porous medium model (Bodvarsson, 1972) using the software ICEBOX. Results for temperature drawdown versus time showed that all three models predict values within 50°C. This illustrated the viability of using a single effective aperture to characterize producer-injector well connections and predict the thermal effect of different injection scenarios.

4.2 INTRODUCTION

Fracture aperture is an important parameter in geothermal reservoirs. Aperture influences transport and thermal behavior of the reservoir, both in EGS and in conventional hydrothermal systems. An important application is to the determination of the degree of interwell connectivity. Of critical importance is the prevention of thermal breakthrough from injection wells to production wells. During the 1980s, several unsuccessful attempts we made to estimate fracture aperture by matching tracer test data. This was because the parameter estimation problem has multiple degrees of freedom, which makes it difficult to separate fracture aperture from other unknown reservoir parameters. To constrain the degrees of freedom, thermal response data could be used. This was proposed in the 1980s, however at the time no data existed that provided both tracer and thermal responses. Now that several EGS and fractured reservoirs have been monitored to provide these data, the possibility now exists to estimate fracture aperture in those fields. In this project, a single fracture model was used to describe the connectivity of an injection and production well

pair. Tracer and thermal data were used to estimate the fracture width for this simplified model.

The objective of the initial work was to determine whether it would be feasible to derive reasonable estimates of the fracture aperture using both thermal and tracer test results. Another objective was to document existing analytical models and field data available in literature. Moreover, calculated fracture width values were compared to those derived from other datasets to check for consistency. Afterwards, aperture values were reevaluated to account for the actual temperature ratio and to correct previous miscalculations. In addition, studies on fracture characterization using acoustic imaging were reviewed to develop a better understanding of feed zone related fractures. Several attempts to simulate flow in a single fracture between wells were done but were not successful.

Focus this quarter has been on understanding the significance of the derived aperture estimates to predicting reservoir behavior. Cooling predictions from the fracture model were compared to those from two versions of porous medium models. One is a porous model with heat loss and the other is a tracer derived model calculated using ICEBOX software (Axelsson, 1995). This was done using data from the Palinpinon geothermal field (Maturgo et al., 2010).

4.3 METHODOLOGY

4.3.1 Analytical Model: Fracture Aperture

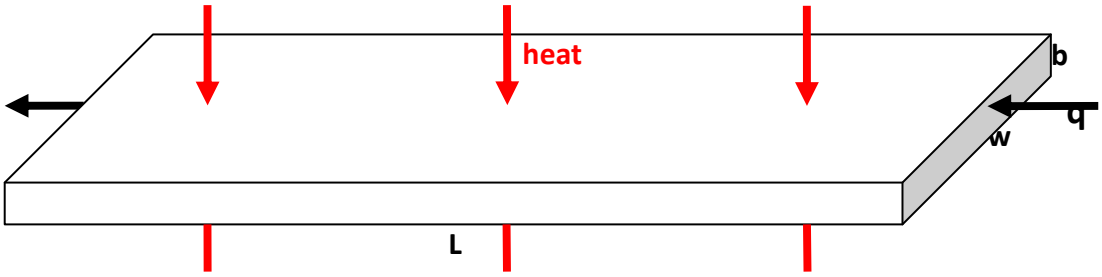

Figure 4.1 Model schematic for the Gringarten and Sauty (1975) derivation

Gringarten and Sauty (1975) derived a solution that can be used for unsteady-state one-dimensional heat transfer through a fracture. The solution was similar to that for a porous medium, derived by Lauwerier (1955). The solution assumes a thin, uniform reservoir with an adiabatic boundary. Heat is transferred by conduction from the rock layers and the entering fluid. Since no mixing is assumed, the result is a stream-like channel flow.

Horne (1996) derived the resulting analytical solution for this model as Equation 4.1 where t_c is the tracer front arrival time, t_{th} is the thermal breakthrough time, and b is the fracture aperture. On the left hand side of Equation 4.1 is the relative temperature ratio T_{ratio}. Here, T_o is the original reservoir temperature, T_w is the reservoir temperature at x, and T_{inj} is the injected fluid temperature. Thus, the fracture aperture can be determined using the thermal

and tracer breakthrough data. Knowledge of the fracture aperture can then be used to predict temperature drawdown in producing wells.

$$T_{ratio} = \frac{T_o - T_w}{T_o - T_{inj}} = erfc\left\{\left[\frac{\phi_w C_w}{K_r \rho_r C_r}\left(\frac{b}{t_c}\right)^2 (t_{th} - t_c)\right]^{-\frac{1}{2}}\right\} \quad (4.1)$$

$$b = \left\{\left(erfc^{-1}\left[\frac{T_o - T_w}{T_o - T_{inj}}\right]\right)^{-2} \frac{t_c^2}{(t_{th} - t_c)} \frac{K_r \rho_r C_r}{\phi_w C_w}\right\}^{1/2} \quad (4.2)$$

These are the analytical expressions used to model a single fracture connection between an injector and producer well pair. Equation 4.2 calculates the effective fracture aperture from the thermal arrival time t_{th}; tracer front arrival time t_c; and relative temperature ratio T_{ratio}.

4.3.2 Available field data

Results from tracer tests in EGS and conventional fractured geothermal reservoirs have been reported frequently in the literature. However, thermal breakthrough data are not as widely published. For EGS fields, thermal data were obtained usually from long-term circulation tests, as for example in Hijiori, Matsunaga et al. (2002) and Matsunaga et al. (2005). Historic silica geothermometer data were used from Palinpinon field, which is a conventional liquid-dominated reservoir, Maturgo at al. (2010). Matsukawa is a conventional vapor-dominated field, Fukuda at al. (2006). Table 4.1 provides a summary of the field data used in this study. The thermal breakthrough time t_{th} here corresponds to the time it takes to reach a T_{ratio} of 0.5.

Table 4.1: Thermal and tracer breakthrough times from field data.

Field	Injector	Producer	t_c	t_{th}	Source
			days	days	
Hijiori	HDR-1	HDR-2A	1	175	Matsunaga et al. (2002)
	HDR-1	HDR-3	4	266	Matsunaga at al. (2005)
Palinpinon	NJ2RD	NJ5D	15	730[1]	Maturgo at al. (2010)
	SG2RD	NJ3D	28	365	
Matsukawa	M-6	M-8	1.5	146	Fukuda at al. (2006)

[1] Assumed that injection in NJ2RD started in 1998 or 1 year before the start of drawdown in NJ5D based on the Palinpinon injection and production history discussed by Bayon and Ogena (2005).

4.3.3 Single Fracture Model: Cooling Rate Prediction

$$T_w = T_o - (T_o - T_{inj})\,erfc\left\{\left[\frac{(\rho_w C_w)^2}{K_r \rho_r C_r}\left(\frac{qb}{A_{tracer}x}\right)^2\left(t - \left(\frac{\rho_A C_A}{\rho_w C_w}\right)\frac{A_{tracer}x}{q}\right)\right]^{-\frac{1}{2}}\right\} \quad (4.3)$$

$$\rho_A C_A = \phi\rho_w C_w + (1-\phi)\rho_r C_r \quad (4.4)$$

$$A_{tracer} = \phi A_{crosssection} \quad (4.5)$$

$$A_{\max} = \frac{q_{total}}{v_{mean}} \quad (4.6)$$

$$q = q_{total}\left(\frac{A_{tracer}}{A_{\max}}\right) \quad (4.7)$$

The general equation for temperature versus time as derived by Gringarten and Sauty (1975) is shown in Equation 4.3. Here, x is the distance between the injection well and producer well. Thus, once the aperture b is determined, this equation describes the cooling of producing feedzones due to injection with constant volumetric rate (q) and temperature (T_{inj}). Note that q specified here is not the total injection rate. It is the rate of effective injected volume that goes to a particular producer. This is approximated by obtaining the ratio of the area derived from tracer analysis to the maximum area based on the total injection rate and the observed mean velocity from tracer data. Equations 4.5 to 4.7 illustrate these in more detail.

4.3.4 Porous Channel with Heat Loss Model: Cooling Rate Prediction

Maturgo et al. (2010) used tracer analysis to determine the effective area (A_{tracer}) for two injector and producer well pairs. These are NJ3D-SG2RD and NJ2RD-NJ5D. Using parameters from the general equation and the effective cross sectional area, thermal velocity without heat loss (v_{th}) can be defined as shown in Equation 4.8. From this definition, Equation 4.3 can be rearranged to get Equation 4.9 which describes the cooling effect of injection for a porous connection model. As explained in the previous section, q is the effective volumetric injection rate.

$$v_{th} = \frac{q}{A_{tracer}}\frac{\rho_w C_w}{\rho_A C_A} = v_w\phi \quad (4.8)$$

$$T_w = T_o - (T_o - T_{inj})\,erfc\left\{\left[\frac{(\rho_A C_A)^2}{K_r \rho_r C_r}\frac{v_{th}^2 b^2}{x^2}\left(t - \frac{x}{v_{th}}\right)\right]^{-\frac{1}{2}}\right\} \quad (4.9)$$

4.4 PRELIMINARY CALCULATIONS AND RESULTS

4.4.1 Fracture Aperture

As described in the previous section, fracture aperture can be estimated directly from the thermal and tracer breakthrough time. Assumptions for the values of the other parameters are listed in Table 4.2. These were the values assigned to these properties in the estimation of fracture aperture. Actual temperature ratios for the injector-producer pairs derived from long term circulation test results are shown in Table 4.3. Estimated fracture aperture values are given in the same table.

To determine the relative temperature for M-6 and M-8 in Matsukawa, a 60°C injection temperature was assumed. Estimates of effective fracture aperture *b* vary from 2.1 cm to 42.6 cm. Though the HDR-1 and HDR-2A well pair in Hijiori exhibited the shortest mean tracer arrival time, it had the lowest calculated effective aperture value because of the long thermal breakthrough time. This observation demonstrates the value of using both tracer and thermal results to constrain the effective aperture. Using this analytical solution also provides an alternative method to characterize the flow path between wells.

Results from finite element heat and mass transfer modeling (FEHM) of the Hijiori field demonstrate fracture aperture values of about 2 mm (Tenma et al., 2005). This is significantly lower than the calculated aperture values. Further investigation of results from aperture estimates from numerical modeling will be undertaken. However, effective fracture aperture derived from acoustic imaging logs show a range of values consistent with those calculated. The next section will describe these studies in detail.

Table 4.2: Assumptions used in calculations.

Rock thermal conductivity	K_r	2	W/m-C
Rock density	ρ_r	2200	kg/m^3
Water density	ρ_w	900	kg/m^3
Rock heat capacity	C_r	0.712	kJ/kg-C
Water heat capacity	C_w	4.342	kJ/kg-C

Table 4.3: Relative temperature ratios and calculated fracture aperture from thermal and tracer breakthrough times.

Field	**Injector**	**Producer**	T_{ratio}	**Calculated *b*** **cm**
Hijiori	HDR-1	HDR-2A	0.46	2.1
	HDR-1	HDR-3	0.14	6.9
Palinpinon	NJ2RD	NJ5D	0.17	15.7
	SG2RD	NJ3D	0.07	42.6
Matsukawa	M-6	M-8	0.29[2]	3.5

[2] Assumed an injection temperature of 60°C

4.4.2 Cooling Predictions

Comparison of cooling predictions was the most convenient way of relating the various producer-injector well connection models to each other. We wanted to investigate if the models would give similar temperature drawdown profiles. Assumptions used for cooling rate calculations are shown in Table 4.4. Area values used to determine the effective injection rate going to the producer are in Table 4.5. These values were used by Maturgo et al. (2010) to predict the temperature drawdown due to injection at a constant rate (q_{total}) and temperature (T_{inj}). Palinpinon was chosen because it had detailed cooling rate calculations available in the literature. This also served as an additional verification of the validity of our models and the results of our calculations.

Table 4.4: Parameters used for cooling rate predictions

Field	Injector	Producer	q_{total}	T_o	T_{inj}	L
			m^3/s	C	C	m
Palinpinon	NJ2RD	NJ5D	0.178	265	160	1500
	SG2RD	NJ3D	0.117	265	160	1500

Table 4.5: Effective injection rate calculation

Field	Injector	Producer	A_{max}	A_{tracer}	q
			m^2	m^2	m^3/s
Palinpinon	NJ2RD	NJ5D	217.5	50.7	0.041
	SG2RD	NJ3D	175.8	39.7	0.027

Cooling rate or temperature drawdown predictions from three models were compared. First was the single fracture model as described in Equation 4.3. Next was the porous model with heat loss using Equation 4.9. The third was the isotropic porous medium model derived by Bodvarsson (1972) calculated using the ICEBOX software (Axelsson, 1995 and Axelsson, 2005). As described in the previous section, calculation of temperature drawdown for the first two models was straightforward. On the other hand, values for the third model were just extracted from the paper where data for aperture calculations were obtained (Maturgo et al., 2010).

Figure 4.2 shows the results for NJ2RD-NJ5D while Figure 4.3 illustrates the forecast for NJ3D-SG2RD. Time in the *x* axis is measured from the start of injection. For NJ2RD-NJ5D, the fracture model gives a prediction very similar to the one using ICEBOX. However, the porous model for this well pair presents a more pessimistic temperature forecast. On the other hand, both the porous model and fracture model agree on a lower stabilized temperature than the ICEBOX model prediction for NJ3D-SG2RD as seen in Figure 4.3. It is still unclear why the three models behaved differently for these two

scenarios. Still, it is good that all three models agree within a range of 50°C. This agreement proves that the effective single fracture aperture model is a viable one because it can be used to predict injection effects. Further investigation using numerical modeling as well as data from other geothermal fields will have to be made.

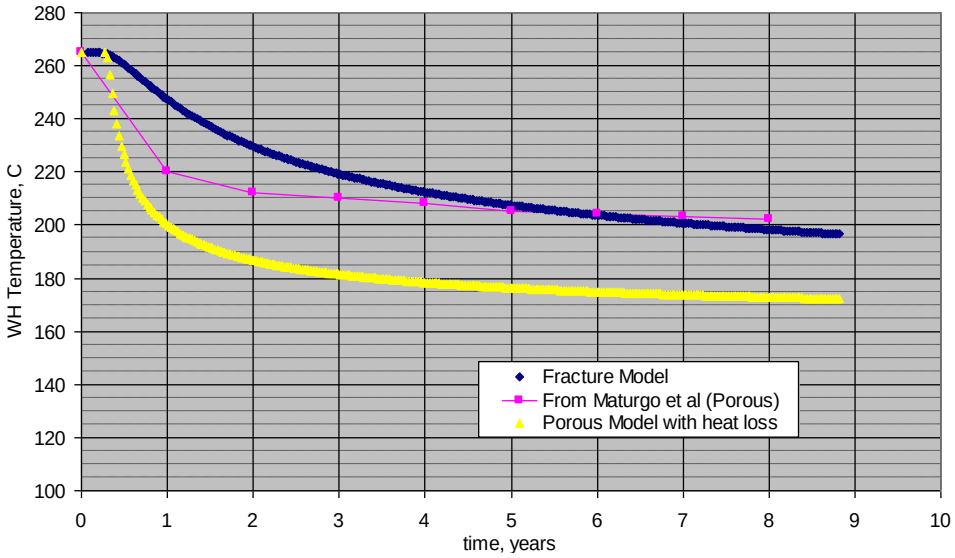

Figure 4.2 Comparison of cooling predictions for NJ2RD-NJ5D from different models: (1) fracture model; (2) porous model with heat loss; (3) ICEBOX (Maturgo et al.,2010).

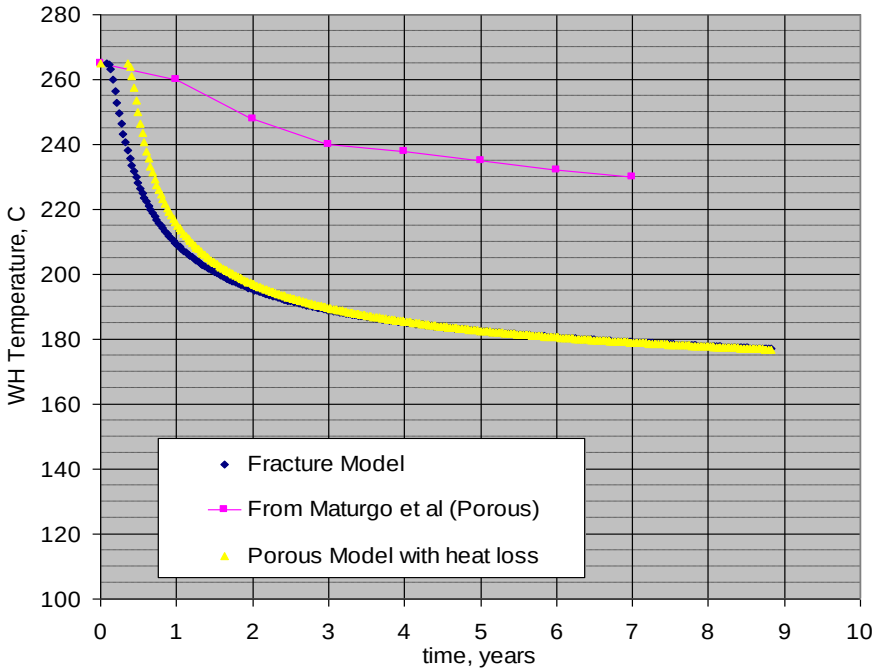

Figure 4.3 Comparison of cooling predictions for NJ3D-SG2RD from different models: (1) fracture model; (2) porous model with heat loss; (3) ICEBOX (Maturgo et al., 2010).

4.5 REVIEW OF RELATED LITERATURE

4.5.1 Acoustic Imaging

Characterization of fluid flow in fractures is an important area of study in geothermal reservoir engineering. Overall permeability in these reservoirs is fault-dominated (Massart, 2010). Relevant fracture parameters to fluid flow are: orientation, aperture, extension, and density. These parameters influence transport and thermal behavior of the reservoir, both in enhanced geothermal systems (EGS) and in conventional hydrothermal systems. Recent advances in borehole imaging technology have made it possible to measure fracture properties with greater accuracy.

For the Wairakei geothermal field, McLean and McNamara (2011) used a high temperature acoustic formation imaging tool (AFIT) to collect fracture data. Confidence, azimuth, and amplitude filters were applied to the data prior to analysis. A borehole televiewer (BHTV) similar to AFIT was also used in the Desert Peak EGS project, in addition to formation microscanner (FMS) image logs (Devatzes and Hickman, 2009).

Published fracture data from various geothermal fields were collected and analyzed. Data sets examined for this study are fracture aperture and density. These were then compared to locations of feed zones to determine their correlation with fluid flow properties.

Fracture data from the various geothermal fields show consistent correspondence between fracture apertures and feed zone locations for most of the data points. In Wairakei, fracture apertures for the feed zones range from around 10 to 60 centimeters in wells WK-404, WK-318, and WK-407 (McLean and McNamara, 2011). A similar trend can be observed from the Desert Peak data (Devatzes and Hickman, 2009. Data for well 27-15 had aperture values from 3 to 10 cm at fluid entry zones. Figures 4.4 to 4.7 show the feed zone locations, PTS data, and fracture apertures for various wells in Wairakei and Desert Peak.

There are two possible explanations for this observation. Using a parallel-plate model, fracture permeability is proportional to b^2, where b is the fracture aperture (Jourde et al., 2002). Fluid entry, associated to fractures in geothermal reservoirs, occurs at depths with high permeability. Therefore, feed zone locations will be at depths with high apertures. Another rationale is the power-law scaling between joint length and width described by Scholz (2010), who argued that for opening mode in rocks, fracture toughness scales linearly with $\sqrt{L}$ and b scales linearly with L, where L is the length. Therefore, a larger fracture width will correspond to a longer fracture which implies a farther reach for the fluid source.

On the other hand, there appears to be no correlation between fracture density and feed zone depths. Massart et al. (1999) analyzed data sets from natural faults and extension fractures and verified that the data follows power-law scaling in multiple-observational scales. Results from their study show that the power-law scaling applies across six ranges of scale within reasonable uncertainty limits. Zones with higher fracture aperture values will have smaller fracture density. Based on this, regions with higher apertures will have

lower fracture density values. Hence, fluid entry points should have lower fracture densities. However, this was not observed consistently in all the data. The lack of inverse correspondence between fracture density and feed zone location could be due to the binning of data. Tool measurement uncertainties could also cause deviations. Moreover, there is inherent error associated with the inverse scaling of fracture density and aperture.

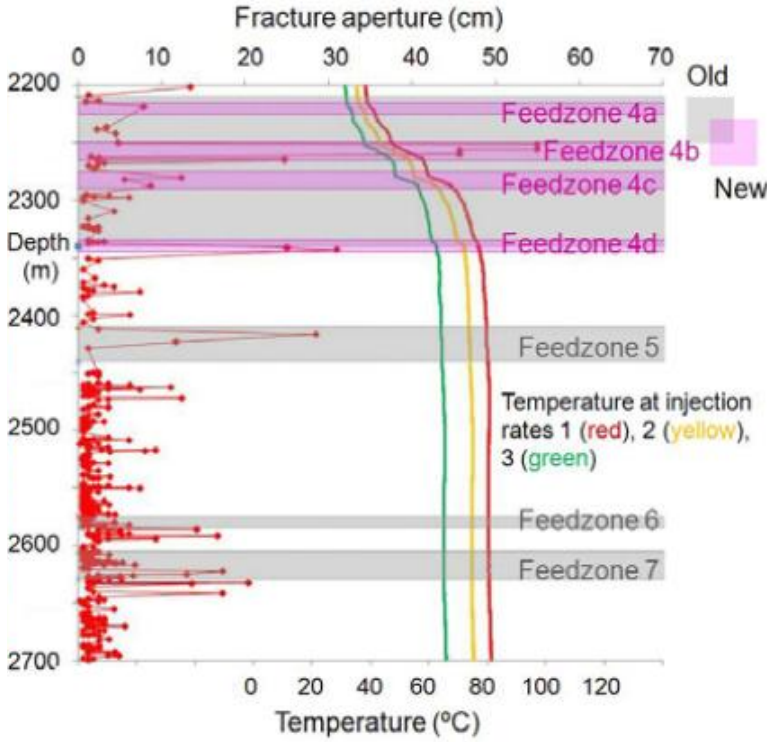

Figure 4.4 Fracture aperture (red) and temperature versus depth for well WK-404 in the Wairakei Geothermal Field (from McLean and McNamara, 2011).

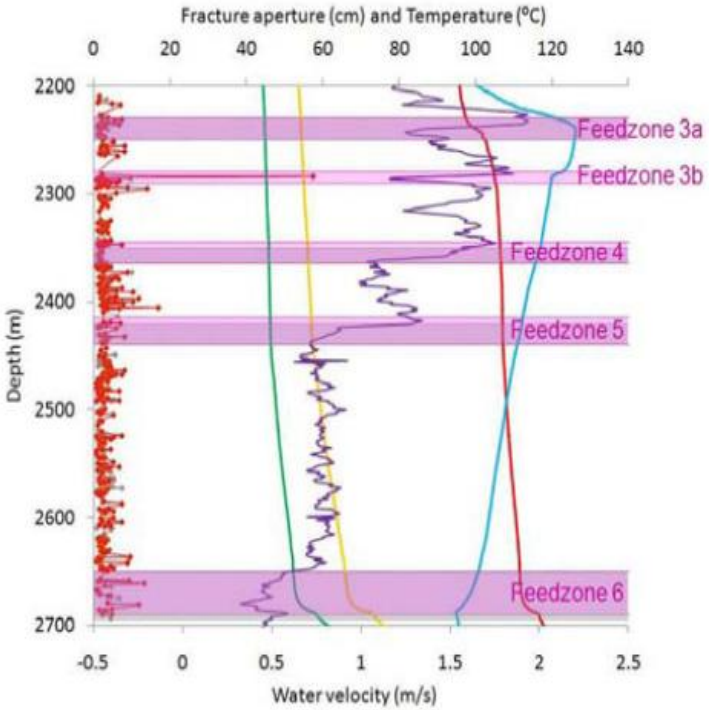

Figure 4.5 Fracture aperture (red), temperature, and spinner velocity (blue) versus depth log for well WK-317 in the Wairakei Geothermal Field (from McLean and McNamara, 2011.

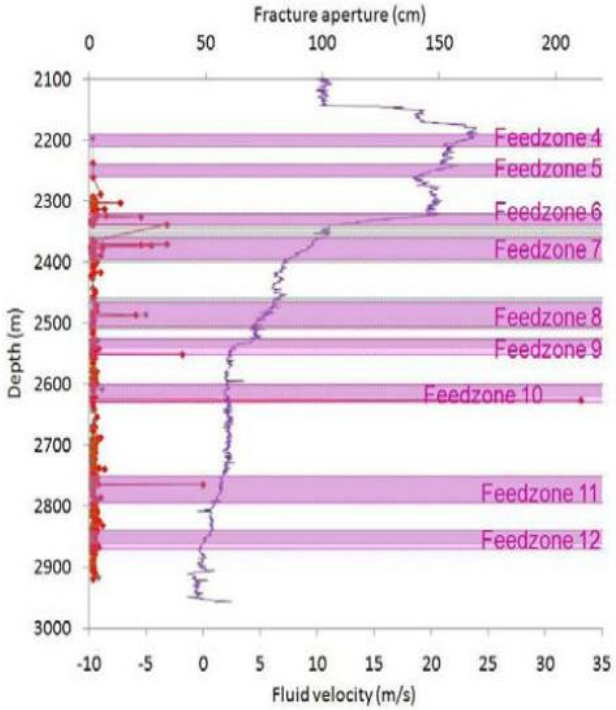

Figure 4.6 Aperture (red) and spinner velocity (blue) versus depth log for well WK-407 in the Wairakei Geothermal Field (from McLean and McNamara, 2011.

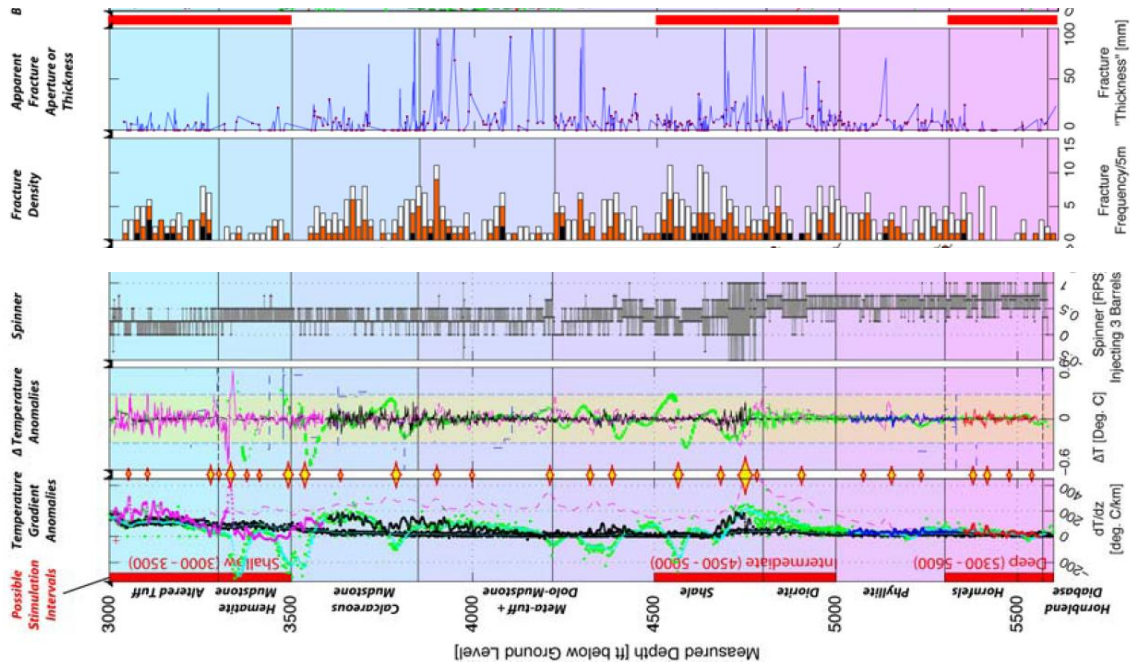

Figure 4.7 Well Log data for well 27-15 in the Desert Peak Geothermal Field, Nevada. Yellow diamonds indicate feed zones derived from temperature anomalies and spinner velocities (from Devatzes and Hickman, 2009).

4.6 FUTURE WORK

Further analysis on this approach to estimating fracture aperture will be undertaken. A review of past studies on fracture characterization using tracer analysis and numerical modeling will be done. Use of pressure transient analysis for fracture characterization will also be explored.

Previous attempts on the use of numerical simulation to model the effect of fracture aperture on mass and heat transport have been met with challenges. Creating this model and comparing it with the analytical results, however, is still endeavored in the future.

5. REFERENCES

Alaskar, M., Ames, M., Horne, R.N., Li, K., Connor, S. and Cui, Y.: "In-situ Multifunction Nanosensors for Fractured Reservoir Characterization," GRC Annual Meeting, Sacramento, USA, vol. 34 (2010).

Alaskar, M., Ames, M., Horne, R.N., Li, K., Connor, S. and Cui, Y.: "Smart Nanosensors for In-situ Temperature Measurement in Fractured Geothermal Reservoirs," GRC Annual Meeting, San Diego, USA, (2011).

Bayon, F.E.B. and Ogena, M.S.: "Handling the Problem of Rapid Reinjection Returns in Palinpinon-I and Tongonan, Philippines," *Proceedings* World Geothermal Congress. 2005.

Bennett, K. and Horne, R. N., Power Generation Potential from Coproduced Fluids in the Los Angeles Basin, *Geothermal Resources Council*, (2011).

Devatzes, N.C. and Hickman, S.H.: "Fractures, stress, and fluid flow prior to stimulation of well 27-15, Desert Peak, Nevada, EGS project," *Proceedings* 34th workshop on Geothermal Reservoir Engineering, Stanford University. 2009.

Devatzes, N.C. and Hickman, S.H.: "In-situ stress and fracture characterization for planning of an EGS stimulation in the Desert Peak Geothermal Field, Nevada," *Proceedings* 35th workshop on Geothermal Reservoir Engineering, Stanford University. 2010.

Dinh, A. V., Interwell Connectivity Tests in Waterflood Systems, *Ph.D. Thesis*, (2009) University of Oklahoma.

Fukuda, D., Akatsuka, T., and Sarudate, M: "Characterization of inter-well connectivity using alcohol tracer and steam geochemistry in the Matsukawa vapor-dominated geothermal field, Northeast Japan," *GRC Transactions*. 2006, 797-801.

Gerber, R., and Birss, R.B.: High Gradient Magnetic Separation. Chichester: Research Studies, 1983.

Gringarten, A.C. and Sauty, J. P.: "A theoretical study of heat extraction from aquifers with uniform regional flow," *Journal of Geophysical Research*. 1975, 4956-122.

Holder, D.S.: Electrical Impedance Tomography: Methods, History and Applications, IOP, UK (2004).

Horne, R.N.: "Reservoir Engineering of Reinjection," Course Notes. Stanford University, 1996.

Jourde, H., Flodin, E.A., Aydin, A., Durlofsky, L.J., and Wen, X.H.: "Computing permeability of fault zones in Eolian sandstone from outcrop measurements," *American Association of Petroleum Geologists Bulletin*. 2002.

"K&J Magnetics - Magnet Calculator." K&J Magnetics - Strong Neodymium Magnets, Rare Earth Magnets. 20 May 2011. <http://www.kjmagnetics.com/calculator.asp>.

Lauwerier, H. A., The transport of heat in an oil layer caused by the injection of hot fluid. *Applied Scientific Research*, **5(2)**, (1955) 145-150.

Lee, K. H., Ortega, A., Jafroodi, N., Ershaghi, I., SPE132625: A Multivariate Autoregressive Model for Characterizing Producer Producer Relationships in Waterfloods from Injection/Production Rate Fluctuations, *SPE Western Regional Meeting*, (2010).

Lovekin, J. and Horne, R. N., Optimization of injection scheduling in geothermal fields, *DOE Research and Development for the Geothermal Marketplace, Proceedings of the Geothermal Program Review VII*, (1989), pp. 45-52.

Marrett, R., Ortega, O., and Kelsey, C.M.: "Extent of power-law scaling for natural fractures in rock," *Geology*. September 1999; v. 27; no. 9; p. 799-802.

Massart, B., Paillet, M., Henrion, V., Sausse, J., Dezayes, C., Genter, A., and Bisset, A.: "Fracture characterization and stochastic modeling of the granitic basement in the HDR Soultz Project (France)," *Proceedings*, World Geothermal Congress. 2010.

Matsunaga, I., Yanagisawa, N., Sugita, H., Tao, H.: "Reservoir monitoring by tracer testing during a long term circulation test at the Hijiori HDR site," *Proceedings*, Twenty-Seventh Workshop on Geothermal Reservoir Engineering, Stanford University. 2002.

Matsunaga, I., Yanagisawa, N., Sugita, H., Tao, H.: "Tracer tests for evaluation of flow in a multi-well and dual fracture system at the Hijiori HDR test site," *Proceedings*, World Geothermal Congress. 2005.

Maturgo, O.O., Sanchez, D. R., and Barroca, G.B.: "Tracer test using naphthalene disulfonates in Southern Negros Geothermal Production Field, Philippines," *Proceedings*, World Geothermal Congress. 2010.

McLean, K. and McNamara, D.: "Fractures interpreted from acoustic formation imaging technology: correlation to permeability," *Proceedings,* 36th workshop on Geothermal Reservoir Engineering, Stanford University. 2011.

Pritchett, J.W.: Finding Hidden Geothermal Resources in the Basin and Range Using Electrical Survey Techniques. A Computational Feasibility Study, report INEEL/EXT-04-02539 (2004).

Pruess, K. and Bodvarsson, G. S.: "Thermal effects of reinjection in geothermal reservoirs with major vertical fractures," *Journal of Petroleum Technology*. 1984, 1567-1578.

Scholz, C.H.: "A note on the scaling relations for opening mode fractures in rock," *Journal of Structural Geology.* 2010.

Singha, K. and Gorelick, S.M. Saline Tracer Visualized with Three-dimensional Electrical Resistivity Tomography: Field-scale Spatial Moment Analysis. *Water Resources Research*, **41** (2005), W05023.

Slater, L., Binley, A.M., Daily, W. and Johnson, R.: Cross-hole Electrical Imaging of a Controlled Saline Tracer Injection. *Journal of Applied Geophysics*, **44**, (2000), 85-102.

Stacey, R.W., Li, K. and Horne, R.N.: Electrical Impedance Tomography (EIT) Method for Saturation Determination, *Proceedings*, 31st Workshop on Geothermal Reservoir Engineering, Stanford University, Stanford, CA (2006).

Tenma, N., Yamaguchi, T., and Zyvoloski, G.: Variation of the characteristics of the shallow reservoir at the Hijiori test site between 90-days circulation test and long-term circulation test using FEHM code." *Proceedings*, World Geothermal Congress. 2005.

Tester, J., Anderson, B., Batchelor, A., Blackwell, D., DiPippo, R., Drake, E., et al., The future of geothermal energy: Impact of Enhanced Geothermal Systems on the United States in the 21st Century, (2006), Massachusetts Institute of Techology.

Ucok, H., Ershaghi, I. and Olhoeft, G.R.: Electrical Resistivity of Geothermal Brines, *Journal of Petroleum Technology*, **32**, (1980), 717-727.

Wang, P. and Horne, R.N.: Integrating Resistivity Data with Production Data for Improved Reservoir Modeling, SPE 59425, SPE Asia Pacific Conference, Yokohama, Japan (2000).